© 2023. Published by The Company of Biologists Ltd | Journal of Cell Science (2023) 136, jcs260327. doi:10.1242/jcs.260327

RESEARCH ARTICLE

CCDC66 regulates primary cilium length and signaling via interactions with transition zone and axonemal proteins

Ezgi Odabasi[1,*], Deniz Conkar[1,*], Jovana Deretic[1], Umut Batman[1], Kari-Anne M. Frikstad[2], Sebastian Patzke[2] and Elif Nur Firat-Karalar[1,3,‡]

ABSTRACT

The primary cilium is a microtubule-based organelle that serves as a hub for many signaling pathways. It functions as part of the centrosome or cilium complex, which also contains the basal body and the centriolar satellites. Little is known about the mechanisms by which the microtubule-based ciliary axoneme is assembled with a proper length and structure, particularly in terms of the activity of microtubule-associated proteins (MAPs) and the crosstalk between the different compartments of the centrosome or cilium complex. Here, we analyzed CCDC66, a MAP implicated in cilium biogenesis and ciliopathies. Live-cell imaging revealed that CCDC66 compartmentalizes between centrosomes, centriolar satellites, and the ciliary axoneme and tip during cilium biogenesis. CCDC66 depletion in human cells causes defects in cilium assembly, length and morphology. Notably, CCDC66 interacts with the ciliopathy-linked MAPs CEP104 and CSPP1, and regulates axonemal length and Hedgehog pathway activation. Moreover, CCDC66 is required for the basal body recruitment of transition zone proteins and intraflagellar transport B (IFT-B) machinery. Overall, our results establish CCDC66 as a multifaceted regulator of the primary cilium and provide insight into how ciliary MAPs and subcompartments cooperate to ensure assembly of functional cilia.

KEY WORDS: CCDC66, Primary cilium, Cilium assembly, Ciliopathy, Centriolar satellite, Axoneme

INTRODUCTION

The primary cilium transduces signaling pathways essential for tissue development and organ homeostasis, including Hedgehog, Wnt and PDGFR signaling (Nachury and Mick, 2019; Wheway et al., 2018). Sensory functions of the cilium require its compartmentalization into structural and functional domains, as well as crosstalk with the centrosome and centriolar satellites (Blacque and Sanders, 2014; Lee and Chung, 2015). The primary cilium has a conserved architecture composed of the microtubule-based axoneme and the ciliary membrane, in addition to distinct subcompartments, such as the transition zone, that have variable structures and functions across different organisms (Blacque and Sanders, 2014; Lee and Chung, 2015). Proximity proteomic studies have identified over 200 proteins as part of the ciliary proteome, although the subciliary localization of the majority is unknown (Kohli et al., 2017; May et al., 2021; Mick et al., 2015). Primary cilium assembly is a tightly regulated, multistep process that involves centriolar maturation to a basal body, elongation of axonemal microtubules from the basal body, formation of the ciliary membrane and establishment of the transition zone (Breslow and Holland, 2019). Precise spatiotemporal control of its assembly kinetics, length, stability, structure and composition are required to ensure proper cilium function. As such, deregulation of these processes causes various human diseases including the multisystem pathologies of the eye, kidney, skeleton, brain and other organs, collectively named 'ciliopathies' (Braun and Hildebrandt, 2017; Reiter and Leroux, 2017). Defining the mechanisms by which a functional cilium is built and maintained is essential to uncover the molecular defects that underlie ciliopathies and their phenotypic heterogeneity.

The transition zone functions as the ciliary gate to control selective ciliary entry and exit of cargoes, and forms structural links between the axoneme and the ciliary membrane (Gonçalves and Pelletier, 2017; Szymanska and Johnson, 2012). Mutations affecting transition zone proteins are prevalent in ciliopathies, highlighting the importance of understanding its biogenesis and function. The transition zone cooperates with multiple protein complexes and cellular structures to regulate cargo trafficking. Intraflagellar transport (IFT)-A and IFT-B machineries and the BBSome complex traffic ciliary proteins along the axoneme between the ciliary base and the tip (Nachury, 2018; Nachury et al., 2007; Nachury and Mick, 2019; Taschner and Lorentzen, 2016). Additionally, membrane-less granules that move around the centrosome, known as centriolar satellites, control cilium composition by regulating protein targeting to basal bodies and cilium (Kodani et al., 2015; Kubo et al., 1999; Odabasi et al., 2020, 2019; Prosser and Pelletier, 2020). They have been proposed to act as trafficking machines for centrosome or cilium proteins, such as IFT-B components (Aydin et al., 2020; Odabasi et al., 2019). Another emerging mechanism for cilium content regulation is ectocytosis of ciliary proteins from the cilium tip, which is the region between the ciliary membrane and the plus ends of the furthest reaching ciliary microtubules (Nager et al., 2017; Phua et al., 2017; Wang and Barr, 2016). The cilium tip has also been implicated in Hedgehog signaling, IFT turnover and remodeling of ciliary microtubules (Chien et al., 2017; Conkar and Firat-Karalar, 2020; He et al., 2014; Pedersen and Akhmanova, 2014). Despite its critical functions, the tip region remains as a poorly characterized ciliary subcompartment with respect to its biogenesis and composition.

The ciliary axoneme provides structural support to the cilium and serves as the track for bidirectional transport of cargoes

[1]Department of Molecular Biology and Genetics, Koç University, Istanbul 34450, Turkey. [2]Department of Radiation Biology, Institute of Cancer Research, OUH-Norwegian Radium Hospital, Oslo N-0379, Norway. [3]School of Medicine, Koç University, Istanbul 34450, Turkey.
*These authors contributed equally to this work

‡Author for correspondence (ekaralar@ku.edu.tr)

E.O., 0000-0002-9660-3062; D.C., 0000-0003-3374-8683; J.D., 0000-0003-2003-1165; U.B., 0000-0003-2591-6704; K.-A.M.F., 0000-0001-9923-3485; S.P., 0000-0001-6821-197X; E.N.F.-K., 0000-0001-7589-473X

Handling Editor: Guangshuo Ou
Received 10 June 2022; Accepted 20 December 2022

Journal of Cell Science (2023) 136, jcs260327. doi:10.1242/jcs.260327

(Conkar and Firat-Karalar, 2020; Mirvis et al., 2018). It is composed of nine radially arranged, remarkably stable doublet microtubules, which are highly modified by posttranslational modifications (PTMs) (Wloga et al., 2017). The plus ends of axonemal microtubules are spatiotemporally regulated in order to maintain proper cilium structure and length. However, relatively little is known about the mechanisms by which the axonemal microtubules of the primary cilium are nucleated and elongated from the centriolar template to give the right length. Given their critical functions in regulating microtubule nucleation, dynamics and stability, microtubule-associated proteins (MAPs) pose as prominent candidates for regulating such events during cilium biogenesis (Bodakuntla et al., 2019; Conkar and Firat-Karalar, 2020).

Several MAPs mutated in ciliopathies have been characterized as being components of the ciliary tip and the axoneme, which provides leads for the dissection of their roles during axonemal assembly and organization (Bodakuntla et al., 2019; Conkar and Firat-Karalar, 2020). For example, CEP104 interacts with CSPP1 and functions during assembly of Hedgehog-competent cilia with proper structure and length (Frikstad et al., 2019). Notably, CEP104 contains a tubulin-binding TOG domain, which promotes microtubule polymerization *in vitro* and is required during ciliary length regulation (Al-Jassar et al., 2017; Das et al., 2015; Rezabkova et al., 2016; Satish Tammana et al., 2013; Yamazoe et al., 2020). Finally, CEP104, together with CCDC66, ARMC9, TOGARAM1 and CSPP1, is part of a protein module mutated in the ciliopathy Joubert syndrome, suggesting that they might work together during cilium biogenesis and function (Latour et al., 2020). Timing and dynamics of their localization to the primary cilium, whether they form functional complexes at cilium, and the nature of their relationship with the axonemal microtubules remain poorly understood.

We previously identified CCDC66 as a MAP that localizes to the centrosome, centriolar satellites and the primary cilium, and regulates cilium formation (Conkar et al., 2017; Gupta et al., 2015; Sharp et al., 2011). CCDC66 stably localizes to the ciliary axoneme, suggesting that it might be a structural component (Conkar et al., 2019). Frameshift mutations of CCDC66 in dogs, and its deletion in mouse cause retinal degeneration and olfactory deficits (Dekomien et al., 2010; Gerding et al., 2011; Murgiano et al., 2020; Schreiber et al., 2018), and CCDC66 was also identified as part of a Joubert module, although Joubert-causative *CCDC66* mutations have not yet been reported (Latour et al., 2020). Together, these findings suggest that CCDC66 is an important regulator of the structure and/or function of the primary cilium. However, its precise ciliary functions and molecular mechanisms of action are unknown.

Here, we used localization, interaction studies and loss-of-function experiments to define the ciliary functions and mechanisms of CCDC66. High resolution and live imaging experiments identified CCDC66 as a new component of the ciliary axoneme and tip and revealed its dynamic compartmentalization at the cilium, basal body and centriolar satellites during cilium assembly and disassembly. Furthermore, CCDC66 interacts with the transition zone protein CEP290 and the MAPs CEP104 and CSPP1. By ensuring proper ciliary recruitment of these proteins, CCDC66 regulates cilium assembly, length and signaling. Our results identify CCDC66 as a new ciliary MAP required for cilium structure and function, and advance our understanding of the coordinated activity of CCDC66 with other MAPs at the axoneme and centrosomal and ciliary subcompartments.

RESULTS

CCDC66 localizes to the ciliary axoneme and tip, and exhibits highly dynamic localization behavior during ciliogenesis

To examine the localization of CCDC66 relative to centrosomal and ciliary subcompartments, we induced ciliogenesis in the previously characterized retinal pigment epithelial cells stably expressing GFP–CCDC66 (from now on denoted RPE1::GFP–CCDC66) by serum starving them for 24 h, and stained with antibodies against proteins at the distal centriole (centrin 3), distal appendages (CEP164), transition zone (CEP290), IFT-B machinery (IFT88), ciliary membrane (ARL13B) and axoneme (acetylated tubulin) (Conkar et al., 2017) (Fig. 1A, Fig. S1A,B). Intensity profile of CCDC66 signal was compared to the intensity profiles of the indicated centrosome and cilium markers (Fig. 1A). CCDC66 localized proximal to CEP164 and centrin 3 at the basal body and to the centriolar satellites around the centrosome (Fig. 1A). Whereas CEP290 was enriched at the transition zone at the distal end of the centrioles, CCDC66 was enriched at the proximal end of the centrioles and the ciliary axoneme (Fig. 1A; Fig. S1B). At the primary cilium, GFP–CCDC66 localized to the axoneme in a punctate manner, in contrast to the relatively homogenous staining of the ciliary membrane marked by the small GTPase ARL13B (Fig. 1A; Fig. S1A). In a fraction of cells, CCDC66 was enriched at the ciliary tip, as indicated by its relative localization to IFT88 and acetylated tubulin (Fig. 1A). These results together show that CCDC66 has co-existing cellular pools, at the basal body, the primary cilium (axoneme and ciliary tip), and at the centriolar satellites, suggesting multiple functions within the centrosome and cilium complex (Fig. 1A,B).

CCDC66 directly binds to microtubules, localizes to the ciliary axoneme, and its ciliary pool is immobile (Conkar et al., 2019; 2017). These findings led us to hypothesize that it might be a structural component of the axoneme. To test this, we examined CCDC66 localization in serum starved RPE1::GFP–CCDC66 cells treated with 0.5% Triton-X, which removes the surrounding ciliary membrane and membrane-associated proteins, including ARL13B, from the axoneme (Nachury et al., 2007). As compared to control cells, detergent-treated cells had an ∼3-fold reduction in their ciliary ARL13B intensity (P<0.0001), whereas ciliary GFP–CCDC66 intensity remained relatively unchanged (Fig. 1C,D). Given its axonemal association, we next asked whether the microtubule-binding activity of CCDC66 is required for CCDC66 to localize to the primary cilium. In prior work, we showed that C-terminal 570–948 residues of CCDC66 binds to MTs in cells and *in vitro* (Batman et al., 2022; Conkar et al., 2017). To test whether this fragment targets CCDC66 to the cilia, we generated RPE1 cell lines stably expressing mNeonGreen (mNG) fusions of full-length CCDC66 and its truncations based on their interaction with microtubules and presence of the CCDC66 domain. (Fig. 1E). mNG fusions of CCDC66, CCDC66 (409–948) and CCDC66 (570–948) localized to the basal body, axoneme and the ciliary tip, while mNG–CCDC66 (1–408) localized only to the basal body (Fig. 1E; Fig. S1C). Taken together, these data indicated that CCDC66 is stably associated with the axoneme and its C-terminal 570–948 amino acid (a.a.) microtubule-binding fragment is sufficient for the basal body and ciliary localization of CCDC66.

To determine how CCDC66 functions in ciliogenesis, we monitored its spatiotemporal localization dynamics in RPE1:: mNG–CCDC66 stable cells transduced with the ciliary membrane marker mScarlet–ARL13B and induced for cilium assembly by serum starvation (Fig. 1F; Movie 1). In unciliated cells,

Journal of Cell Science (2023) 136, jcs260327. doi:10.1242/jcs.260327

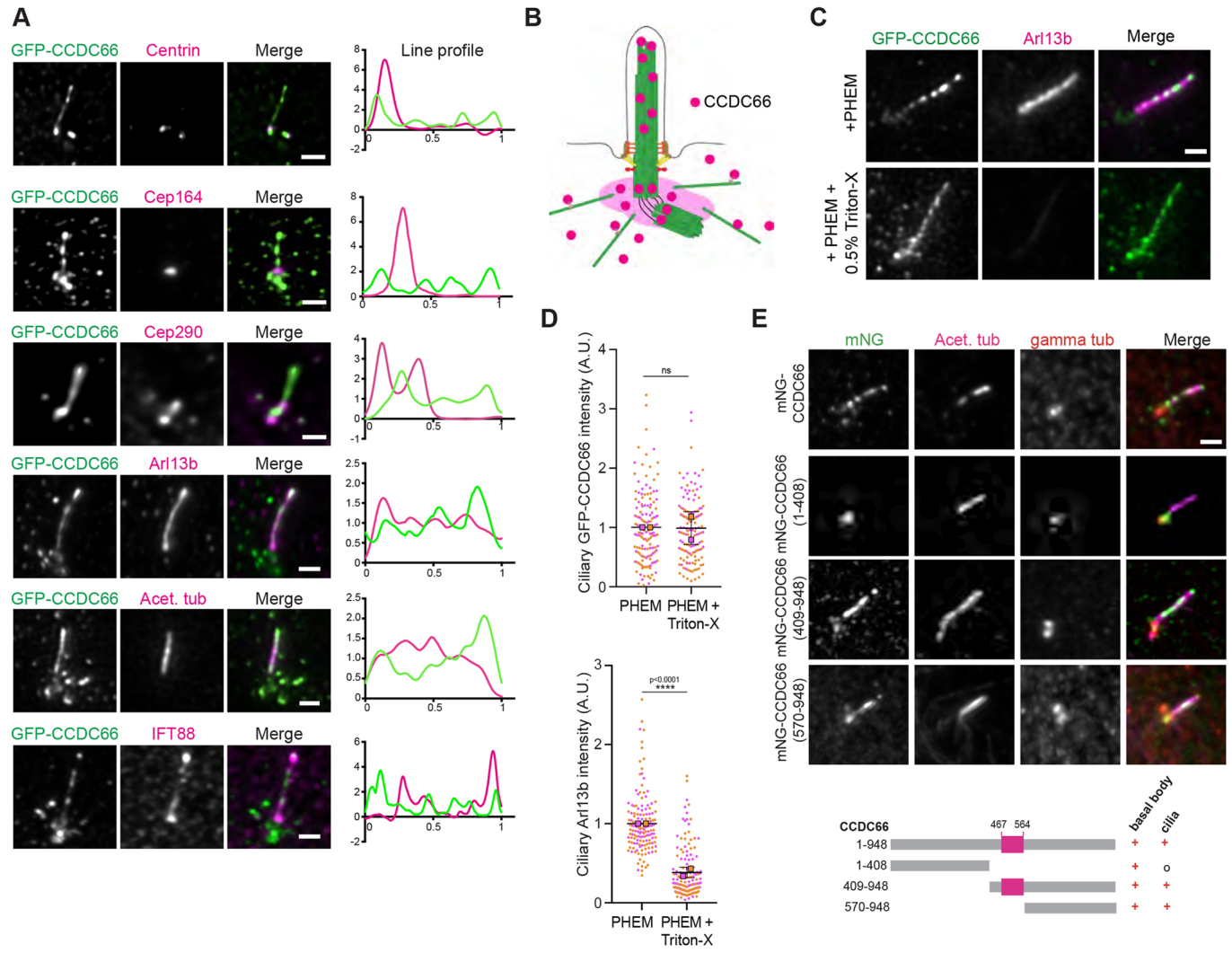

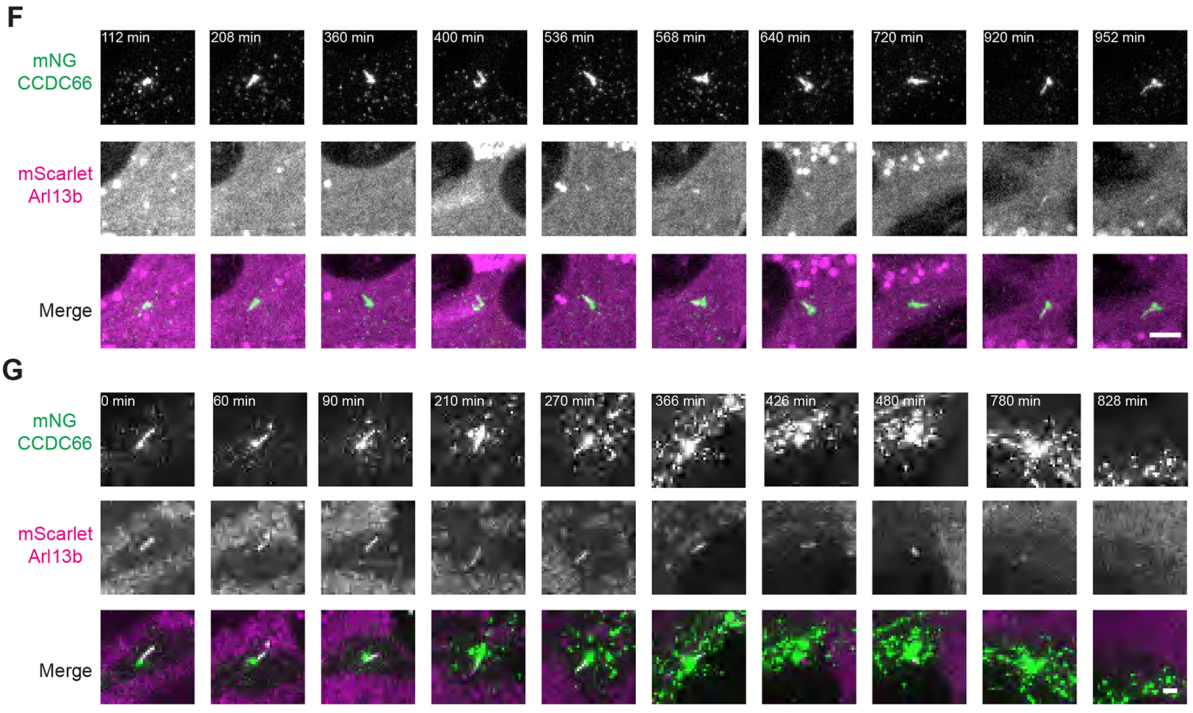

Fig. 1. See next page for legend.

Journal of Cell Science

Journal of Cell Science (2023) 136, jcs260327. doi:10.1242/jcs.260327

Fig. 1. CCDC66 exhibits highly dynamic spatiotemporal dynamics during cilium assembly and disassembly. (A) Sub-centrosomal and-ciliary localization of CCDC66 in ciliated cells. RPE1::GFP–CCDC66 cells were serum starved for 48 h, fixed and stained for GFP along with centriole (centrin), distal appendage (CEP164), transition zone (CEP290) and primary cilium [ARL13B, acetylated tubulin (Acet. tub) and IFT88] markers. Scale bars: 5 µm (acetylated tubulin image), 1 µm (rest of the images). (B) Schematic representation of CCDC66 localization at the centrosome and cilium complex. CCDC66 localizes to the ciliary axoneme and tip, the basal body and the centriolar satellites. It is excluded from the transition zone at the primary cilium. (C,D) CCDC66 stably associates with the ciliary axoneme. (C) Ciliated RPE1::GFP-CCDC66 cells were treated with PHEM or PHEM plus 0.5% Triton-X for 30 s, fixed with PFA and stained for GFP and ARL13B. Scale bar: 5 µm. (D) Ciliary GFP–CCDC66 and ARL13B intensities were quantified by measuring corresponding ciliary intensities and subtracting the background signal. Magenta and orange represent individual values from two independent experiments. Error bars are mean±s.d. (70 cilia/experiment). A.U., arbitrary units. ****P<0.0001; ns, not significant (unpaired two-tailed *t*-test). (E) C-terminal microtubule binding fragment of CCDC66 localizes to the basal body and the axoneme. RPE1::mNeonGreen (mNG)–CCDC66, RPE1::mNG–CCDC66 (1–408), RPE1::mNG-CCDC66 (409–948) and RPE1::mNG-CCDC66 (570–948) (see lower diagram) cells were serum starved for 48 h, fixed and stained for mNG, acetylated tubulin and γ-tubulin. Scale bar: 2 µm. In the diagram, o represents no localization, + represents localization to basal body or cilia. (F) Spatiotemporal dynamics of CCDC66 during cilium assembly. RPE1::mNG–CCDC66, mScarlet–ARL13B cells were imaged with confocal microscopy at 8 min intervals after serum withdrawal. The first time point (112 min) indicates the start of cilium formation. Scale bar: 5 µm. (G) Spatiotemporal dynamics of CCDC66 during cilium disassembly. RPE1::mNG–CCDC66, mScarlet–ARL13B cells were serum starved for 48 h and imaged with confocal microscopy at 6 min intervals after serum addition. Scale bar: 2 µm. Images in A, E–G are representative of two biological repeats.

mNG–CCDC66 localized to the centriolar satellites and centrosome. Following serum starvation, mNG–CCDC66 localized to the growing ciliary axoneme, which was followed by recruitment of mScarlet–ARL13B (Fig. 1F). During cilium assembly, the number of CCDC66-positive centriolar satellites gradually decreased and became less concentrated around the basal body (Fig. 1F). All ciliated cells exhibited ciliary localization of CCDC66 after ARL13B-positive cilia formed, and CCDC66 was retained at the cilia after its recruitment. Analogous to its localization profile in fixed cells, ciliary mNG–CCDC66 was heterogeneously distributed along the cilium and enriched at the cilium tip. Growing or steady state mNG–CCDC66-postive cilia were present in about 80% cells after 24 h serum starvation. Notably, the timing of initiation of ciliogenesis as well as the duration between initiation and formation of steady state cilia after serum starvation varied from cell to cell (Fig. S1D). We confirmed these observations through immunofluorescence analysis of mNG–CCDC66 localization relative to ciliary membrane, axoneme and centriolar satellites in RPE1 cells fixed at different time points after serum starvation (Fig. S1E,F). Thus, CCDC66 localizes to the primary cilium during the initial stages of cilium formation and is a constitutive resident of the cilium and the cilium tip.

We next monitored CCDC66 localization dynamics during cilium disassembly. RPE1::mNG–CCDC66 and mScarlet–ARL13B double-expressing cells were serum starved for 48 h and imaged following serum addition (Fig. 1G; Movie 2). Consistent with described mechanisms of cilium disassembly (Mirvis et al., 2019), the ciliary pools of CCDC66 and ARL13B were lost by multiple different events including ciliary decapitation, resorption of the axoneme and whole-cilium shedding (Fig. 1G; Fig. S1G,H). Notably, in the reverse order to what is seen during cilium assembly, as the axonemal pool of CCDC66 disappeared, the centriolar satellite pool reappeared, suggesting possible redistribution of CCDC66 from cilium to the satellites. We also observed that CCDC66 accumulated at the centrosome during cilium disassembly, supporting the idea that it relocates. Immunofluorescence analysis of cells fixed and stained at different time points after serum stimulation supported these observations (Fig. S1H). Collectively, our results show that CCDC66 enters the primary cilium early during its assembly, stably localizes to the axoneme and ciliary tip, and exits the cilium during its disassembly.

CCDC66 is required for assembling primary cilium with proper length

Our previous work indicated a role of CCDC66 during primary cilium assembly (Conkar et al., 2017). However, the precise roles of CCDC66 during cilium assembly and maintenance is unknown. To address this, we first investigated how CCDC66 affects the kinetics of cilium biogenesis using siRNA-mediated loss-of-function experiments. We quantified the percentage of control and CCDC66-depleted cells that formed cilia over a 48 h serum starvation time course by staining for acetylated tubulin (Fig. 2A; Fig. S2A,B). The fraction of ciliated cells was reduced upon CCDC66 depletion at all time points after serum starvation and did not reach control levels even at 48 h post serum starvation (Fig. 2B). Additionally, we stained cells with proliferation marker Ki-67 (also known as MKI67) and found that the percentage of quiescent CCDC66-depleted cells (Ki-67-negative cells) was comparable to control (Fig. S2C,D). These data shows that failure to enter quiescence does not account for the defective ciliation of CCDC66-depleted cells. Finally, we quantified the effects of CCDC66 loss on cilium length. Cilia that formed in CCDC66-depleted cells were significantly shorter relative to those in control cells at all time points following serum starvation (Fig. 2C). Thus, CCDC66 is required for both the initiation of cilium assembly and elongation of the axoneme.

To spatiotemporally define the cilium elongation defects, we performed live imaging of control and CCDC66 siRNA-transfected RPE1 cells stably expressing the mCitrine fusion of the ciliary transmembrane protein Smoothened (mCitrine–SMO), which marks the cilium (Fig. 2D). After the cells committed to cilia formation, cilia grew slower in CCDC66-depleted cells relative to control cells. By 10 h, the average length of cilia in control cells and CCDC66-depleted cells were ∼3.2 µm and ∼2.7 µm, respectively (Fig. 2D). Notably, the kinetics of cilia growth and shortening at steady state was fairly evenly balanced in control cells, whereas there were more length variations in CCDC66-depleted cells (Fig. 2D). We also examined the behavior of steady state cilia using live imaging by quantifying the following three events from videos: (1) ectocytosis or decapitation from cilium tips, (2) breakage (scission), which represents the thinning of the distal axoneme followed by its breakage, and (3) ripping off, where the cilium starts to elongate abnormally and rips off from a point of enriched mCitrine–SMO signal (Fig. S2E). The percentage of ciliary ectocytosis or decapitation events decreased from 67% in control ciliated cells to 60% in CCDC66-depleted ones (Fig. S2F). CCDC66-depleted cilia also showed an increase in the frequency of tip breakage and scission. Although these differences might also underlie the shorter cilium phenotype, they were not statistically significant.

Cilium assembly and maintenance require remodeling of the microtubule cytoskeleton by a diverse array of MAPs and tubulin PTMs (Broekhuis et al., 2013; Keeling et al., 2016;

Journal of Cell Science (2023) 136, jcs260327. doi:10.1242/jcs.260327

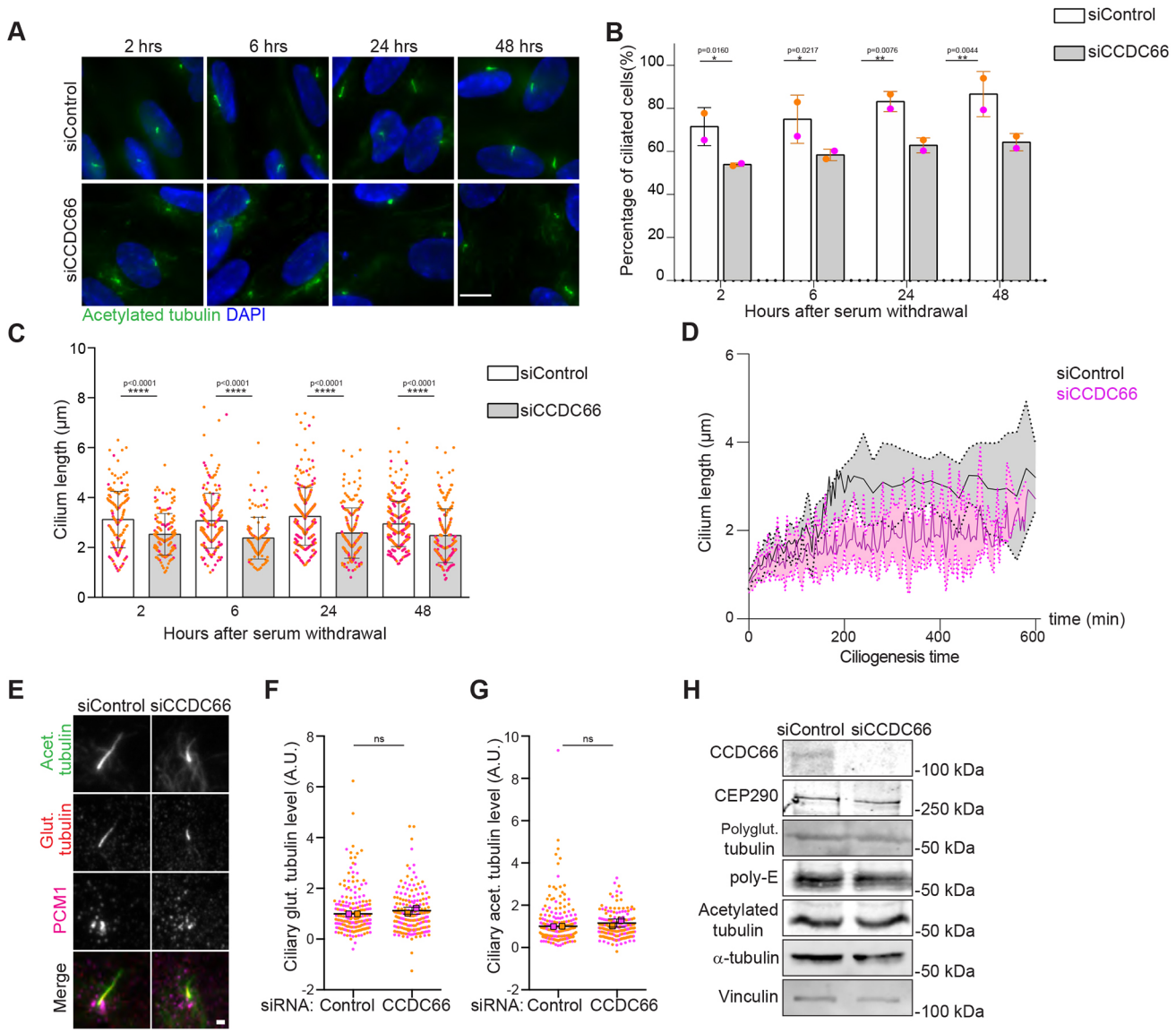

Fig. 2. CCDC66 is required for efficient ciliogenesis and axoneme elongation. (A,B) CCDC66 loss impairs cilium formation. (A) Control and CCDC66-depleted RPE1 cells were fixed at 2, 6, 24 and 48 h after serum starvation. Following fixation, cells were stained for anti-acetylated tubulin antibody and DAPI. Scale bar: 10 µm. (B) The percentage of cilium formation was quantified by dividing the cilium number determined by counting acetylated tubulin by the total cell number determined by counting nuclei, and plotted against time after serum starvation. Magenta and orange represent individual values from two independent experiments. Error bars represent mean±s.d. (100 cells/serum starvation time point for each experiment) **P*<0.05, ***P*<0.01 (two-way ANOVA with Tukey's post hoc test). (C) CCDC66 depletion leads to shorter cilia. Ciliary length from A was measured and plotted against time after serum starvation. Magenta and orange represent individual values from two independent experiments. Error bars represent mean±s.d. (100 cilia/serum starvation time point for each experiment). *****P*<0.0001 (two-way ANOVA with Tukey's post hoc test). (D) CCDC66 depletion results in defective axoneme elongation. RPE1::mCitrine–SMO cells were transfected with two rounds of control or CCDC66 siRNAs. At 48 h post transfection, they were monitored by time lapse imaging over 24 h every 4 min. Lengths of cilia were measured from two independent experiments as SMO-positive cilia appeared (*t*=0). Data represent the mean±s.d. from 22 cilia for siControl and 19 cilia for siCCDC66 from two independent experiments. (E–G) CCDC66 loss does not alter ciliary acetylation and polyglutamylation. (E) RPE1 cells were transfected with two rounds of control or CCDC66 siRNA and serum starved for 48 h. Cells were fixed and stained for acetylated tubulin, polyglutamylated tubulin and PCM1. Scale bar: 1 µm. (F) Ciliary acetylated tubulin and (G) polyglutamylated tubulin levels were quantified from E by measuring the PTM intensities via subtracting the background signal, multiplied by the signal area, and dividing by the cilium length. Data represent the mean±s.d. Magenta and orange represent individual values from two independent experiments (100 cilia/experiment). A.U., arbitrary units. ns, not significant (unpaired two-tailed *t*-test). (H) Effects of CCDC66 depletion on cellular abundance of various proteins. RPE1 cells were transfected with two rounds of control or CCDC66 siRNA and serum starved for 48 h. Cell lysates were prepared, resolved on SDS-PAGE and immunoblotted for CCDC66, CEP290, polyglutamylated tubulin, poly-E, acetylated tubulin, alpha-tubulin and vinculin (loading control). Blot shown representative of two biological replicates.

Pedersen et al., 2012). To examine whether CCDC66 loss results in defective modification of the ciliary tubulin proteins, we quantified ciliary polyglutamylated and acetylated tubulin levels and found that their levels were similar in control and CCDC66-depleted cells (Fig. 2E–G). Cellular levels of polyglutamylated and acetylated tubulin were comparable between control and CCDC66-depleted cells (Fig. 2H). Collectively, these findings identify CCDC66 as a regulator of cilium length.

Journal of Cell Science (2023) 136, jcs260327. doi:10.1242/jcs.260327

CCDC66 depletion interferes with transition zone recruitment of CEP290 and basal body recruitment of the IFT-B machinery

To investigate how CCDC66 regulates ciliogenesis, we used quantitative immunofluorescence to analyze whether known regulators of different stages of ciliogenesis are properly recruited to the centrosomes or cilia upon RNAi-mediated knockdown of CCDC66. To this end, control and CCDC66-depleted cells were serum starved for 48 h and stained for antibodies against components of distal appendages, transition zone proteins and IFT machinery (Fig. 3B–S).

During ciliogenesis, distal appendage protein CEP164 recruits the kinase TTBK2, which phosphorylates CEP83 and MMP9, and results in removal of the centriole capping protein complex CP110–CEP97 from the mother centriole (Čajánek and Nigg, 2014; Graser et al., 2007; Tanos et al., 2013). Whereas CCDC66 depletion resulted in a minor 6% reduction in centrosomal CEP164 levels, it did not alter centrosomal TTBK2 levels (Fig. 3B–E). There was also no defect in the removal of CP110 from the mother centriole upon CCDC66 loss (Fig. 3F,G). These results indicate that CCDC66 is not required for acquisition of distal appendages or removal of the centriole cap.

Centriole cap removal is followed by periciliary vesicles docking to the basal body and their fusion, formation of the transition zone and elongation of the axoneme (Breslow and Holland, 2019). We previously showed that CCDC66 interacts with the transition zone protein CEP290, which plays critical roles in transition zone assembly and ciliary content regulation (Betleja and Cole, 2010; Drivas and Bennett, 2014). The transition zone consists of the membrane-associated or non-membranous NPHP, MKS and CEP290 modules, which form hierarchically (Fig. 3H) (Garcia-Gonzalo and Reiter, 2017; Gonçalves and Pelletier, 2017). To assess how CCDC66 loss affects these modules, we quantified the basal body levels of one protein from each module, namely TCTN1, CEP290 and MKS3 (Fig. 3I–N). Whereas CCDC66 depletion did not alter basal body TCTN1 levels (Fig. 3K,L), there was an ∼0.5-fold decrease in CEP290 (Fig. 3I,J) and a 1.3-fold increase in MKS3 levels at the basal body (Fig. 3M,N). Immunoblotting revealed similar cellular levels of CEP290 between control and CCDC66-depleted cells, indicating that CCDC66 regulates CEP290 targeting to the transition zone (Fig. 2H). These defects suggest that CCDC66 might take part in transition zone assembly by governing proper targeting of specific proteins to the transition zone.

After transition zone assembly, the axoneme is templated from the centriolar base, and the mature cilium is assembled. This process requires proper activity of the IFT machinery, which traffics proteins, such as tubulin dimers, along the ciliary axoneme (Prevo et al., 2017). Therefore, we examined the recruitment of the IFT-B machinery to the basal body and cilium as putative mechanisms that might underlie the ciliary defects of CCDC66-depleted cells (Fig. 3O–S). To this end, we measured the levels of the IFT-B components IFT88 and IFT81 at the cilium ciliary tip and basal body. Although the ciliary tip levels of IFT88 and IFT81 remained unaltered, their basal body levels but not ciliary levels were lower in CCDC66-depleted cells (Fig. 3P,S). These results identify a function for CCDC66 during basal body recruitment of the IFT-B machinery.

Distinct cellular pools of CCDC66 are required for its functions during cilium and transition zone assembly

To address whether and how the ciliary functions of CCDC66 are governed by its distinct cellular pools (at the basal body, centrosomes and primary cilium), we performed phenotypic rescue experiments with four different CCDC66 siRNA-resistant mutants we designed based on their localization and interaction profiles (Fig. 4A): (1) mNG–CCDC66, to validate the specificity of the phenotypes; (2) mNG-CCDC66 (570–948), to assess the functional significance of CCDC66 localization to the basal body and axoneme; (3) mNG-CCDC66 (409–948), to assess the functional significance of CCDC66 interactions with CSPP1, CEP104, PCM1 and CEP290; and (4) an mNG–CCDC66 fusion with the centrosomal localization sequence of AKAP450 (PACT domain) at its C-terminus, to distinguish its centrosome-specific activities from the ones mediated by satellites and the axoneme. For these experiments, we generated RPE1 cell lines stably expressing only mNG, as a control, and mNG fusions of CCDC66 mutants and validated expression of the fusion proteins by blotting cell extracts with antibodies against mNG and CCDC66 (Fig. S3A). Additionally, we examined localization of the fusion proteins in serum-starved, CCDC66-depleted stable cells stained for acetylated tubulin and γ-tubulin. Both mNG–CCDC66, mNG–CCDC66 (570–948) and mNG–CCDC66 (409–948) localized to the basal body, axoneme and the ciliary tip. In agreement with the strong affinity of the PACT domain to the centrosome, mNG-CCDC66-PACT localization was restricted to the centrosomes (Fig. 4A; Fig. S3B).

Using these RPE1 stable lines, we performed rescue experiments for defective cilium assembly, axonemal elongation and targeting of CEP290 to the transition zone in CCDC66-depleted cells. mNG-CCDC66 expression rescued all three phenotypes to comparable levels to control siRNA-transfected mNG-expressing cells, demonstrating that these phenotypes are specific to CCDC66 depletion (Fig. 4B–E). mNG–CCDC66 (570–948), mNG-CCDC66 (409–948) and mNG–CCDC66–PACT partially rescued the reduced ciliation defect (Fig. 4B), suggesting that different CCDC66 pools cooperate during cilium assembly. mNG–CCDC66 (409–948) rescued the shorter cilium phenotype as much as mNG–CCDC66 [2.63±0.81 µm for (408–948), 2.73±0.88 µm for full length; mean±s.d.]; however, mNG–CCDC66 (570–948) partially rescued the shorter cilium phenotype (2.3±0.75 µm) (Fig. 4C). Thus, the functional complexes formed by 409–948 a.a. fragment and the microtubule affinity of the 570–948 a.a. fragment are required to fully rescue the shorter cilium length phenotype. Finally, centrosomal CEP290 levels were restored by expression of mNG–CCDC66–PACT and mNG–CCDC66 (409–948), but not mNG–CCDC66 (570–948) (Fig. 4D,E). These rescues can be explained by the ability of mNG–CCDC66 (409–948) to interact with CEP290 (Fig. 5A) and that CCDC66–PACT might have created more binding sites for CEP290 at the centrosome. To examine the specificity of CEP290 tethering to the centrosome by CCDC66–PACT, we quantified the consequences of its expression on the centrosomal abundance of various centriolar satellite proteins and found that it had variable effects, including an increase for CEP63, decrease for PCM1 and CEP131, and no change for centrin 3 (Fig. S3C). Taken together, results from rescue experiments support that CCDC66 functions during cilium assembly and axoneme elongation require cooperative activity of its distinct cellular pools at the microtubules, cilium and basal body.

CCDC66 cooperates with the ciliopathy proteins CSPP1 and CEP104 during cilium length regulation

To gain insight into how CCDC66 regulates cilium length, we identified its proximity interaction partners in ciliated IMCD3 cells. We used IMCD3 cells as they ciliate with high efficiency and have

Journal of Cell Science (2023) 136, jcs260327. doi:10.1242/jcs.260327

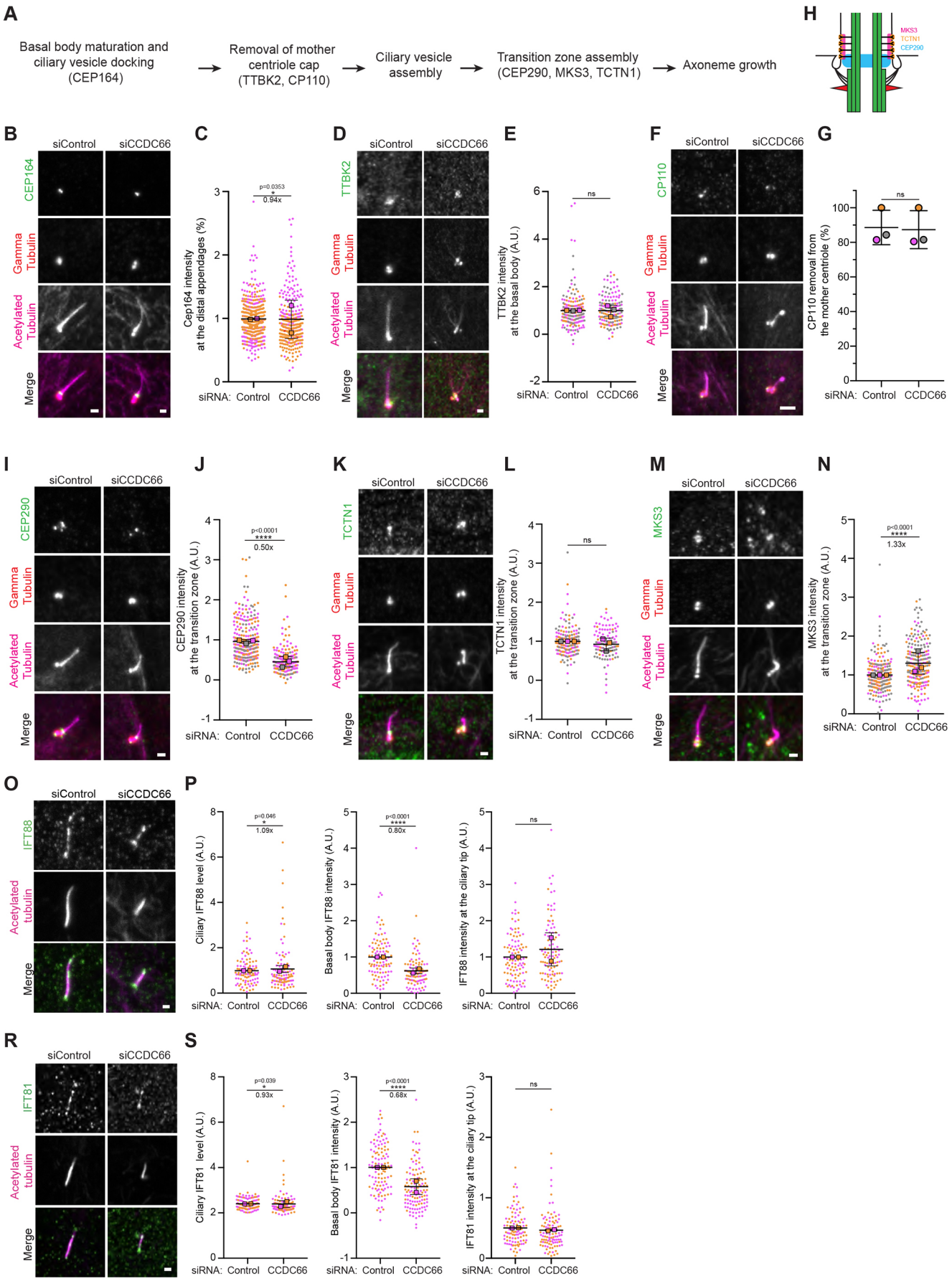

Fig. 3. See next page for legend.

Fig. 3. CCDC66 is important for proper transition zone formation and IFT-B localization to the basal body. (A) Stepwise assembly of the primary cilium and cartoon representation of three transition zone modules. (B–N) CCDC66 loss impairs CEP290 and MKS3 levels at the transition zone. RPE1 cells were transfected with two rounds of control or CCDC66 siRNA and serum starved for 48 h. Cells were fixed and stained for (B) CEP164, (D) TTBK2, (F) CP110, (I) CEP290, (K) TCTN1, or (M) MKS3, and γ-tubulin and acetylated tubulin. (H) Cartoon representation of three transition zone modules. CEP164 levels at the distal appendages, basal body TTBK2 levels, CP110 removal from the mother centriole, CEP290, TCTN1 and MKS3 levels at the transition zone were quantified and plotted. To quantify only transition zone pool of the protein, γ-tubulin is taken as reference. The pools of the CEP290, TCNT1 and MKS3 above the γ-tubulin were quantified as transition zone. Data represent the mean±s.d. Magenta, orange and gray represent individual values from three independent experiments (100 cells/experiment). ****P<0.0001; ns, not significant (unpaired two-tailed *t*-test). Scale bars: 2 µm (B,D,F), 1 µm (I,K,M). A.U., arbitrary units. (O–S) Basal body levels of IFT-B components decrease upon CCDC66 depletion. RPE1 cells were transfected with two rounds of control or CCDC66 siRNA and serum starved for 48 h. Cells were fixed and stained for (O) IFT88 and (R) IFT81 and acetylated tubulin. (P–S) Ciliary, basal body and ciliary tip levels of IFT88 and IFT81 are plotted. Ciliary IFT81 and IFT88 levels were quantified by measuring the protein intensity at cilia, subtracting the background signal, multiplied by the signal area, and dividing by the cilium length. Ciliary IFT81 and IFT88 levels were normalized relative to the mean of control (=1). Data represent the mean±s.d. Magenta and orange represent individual values from two independent experiments (100 cells/experiment). *P<0.01, ****P<0.0001, ns, not significant (unpaired two-tailed *t*-test). Scale bars: 2 µm.

been used in proteomics studies of the primary cilium, which makes benchmarking easier (May et al., 2021; Mick et al., 2015). We generated IMCD3 cells stably expressing FLAG-miniTurbo–CCDC66 or FLAG–miniTurbo (control) using the Flip-IN system. As assessed by streptavidin staining, miniTurbo-CCDC66 biotinylated proteins at the centrosome and centriolar satellites in cycling cells and at centriolar satellites, the basal body and the cilium in serum-starved cells (Fig. S4A). Control cells expressing FLAG-miniTurbo exhibited biotinylation at the cytoplasm.

After validation of the cell lines, we performed large-scale streptavidin pulldown of biotinylated proteins from cells serum starved for 48 h, analyzed them by mass spectrometry (Table S1) and defined high confidence CCDC66 interactome using Normalized Spectral Abundance Factor (NSAF) analysis (Firat-Karalar et al., 2014). Analysis of this interactome by combining Gene Ontology (GO) analysis combined with literature mining revealed enrichment of centrosome, cilium and satellite proteins, MAPs, actin-binding proteins and proteins implicated in microtubule nucleation, which was visualized by Cytoscape (Fig. S4B). Notably, a number of these proximity interactors stood out by their known relationship to CCDC66 or involvement in cilium assembly and function. In addition to Joubert-linked proteins, proteins mutated in retinal degeneration including tubulin tyrosine ligase like 5 (TTLL5), LCA5 and RPGRIP1L were identified (Bedoni et al., 2016; den Hollander et al., 2007; Sergouniotis et al., 2014; Wiegering et al., 2018). Notably, the ciliated CCDC66 interactome did not include CEP290, which was previously identified as part of its interactome in asynchronous cells (Conkar et al., 2017; Gheiratmand et al., 2019; Gupta et al., 2015). Finally, CSPP1, ARMC9, CEP104 and TOGARAM1, which are axonemal proteins required for cilium length control (Das et al., 2015; Frikstad et al., 2019; Latour et al., 2020), were identified in the proximity list of CCDC66 in ciliated cells. Recent studies have defined the tubulin-binding TOG-domain-containing protein CEP104 as a potential axonemal polymerase and showed that it forms a functional complex with CSPP1 during cilium biogenesis (Frikstad et al., 2019; Yamazoe et al., 2020). To examine whether CCDC66 regulates cilium length by cooperating with CSPP1 and CEP104, we investigated the nature of their relationship by immunoprecipitation, loss-of-function and phenotypic rescue experiments.

First, we examined whether they physically interact by performing immunoprecipitation experiments in cells expressing GFP–CCDC66. CSPP1 and CEP104 and known CCDC66 interactors PCM1 and CEP290 co-pelleted with GFP–CCDC66, but not with the negative control GFP (Fig. 5A). Although GFP–CCDC66 (409–948) interacted with PCM1, CSPP1, CEP104 and CEP290, GFP–CCDC66 (570–948) and GFP–CCDC66 (1–408) that lacks the 'CCDC66 domain (408–564 a.a.)' did not. These data suggest that the CCDC66 domain conserved across CCDC66 homologs is required for the ability of CCDC66 to interact with these proteins. Of note, GFP–CCDC66 (1–594) had reduced interaction with PCM1 and CSPP1 and did not interact with CEP104 and CEP290, suggesting that the C-terminal 570-948 a.a. region also contributes to the interaction of CCDC66 with these proteins.

We next asked whether satellites and cytoplasmic microtubules are required for the ability of CCDC66 to interact with CEP290, CSPP1 and CEP104. As compared with control cells, loss of satellites by knocking out PCM1 compromised the interaction of GFP–CCDC66 with CSPP1 and CEP290, but not with CEP104 (Fig. S4C). We note that the CEP290 association defect might be due to reduced levels of total cellular CEP290 in PCM1$^{-/-}$ cells (Fig. S4C). In contrast to loss of satellites, depolymerization of cytoplasmic microtubules by nocodazole treatment did not interfere with the ability of GFP–CCDC66 to interact with CSPP1 and CEP104 (Fig. S4D). Collectively, these results suggest that CCDC66 might interact with CSPP1 and CEP104 at the basal bodies and/or cilium where they might cooperate during cilium assembly and axoneme length regulation.

To examine the dependency of CCDC66, CEP104 and CSPP1 on each for ciliary localization, we performed loss-of-function experiments in RPE1 cells stably expressing their fluorescent fusions (Conkar et al., 2017; Frikstad et al., 2019). We depleted CEP104 and CSPP1 using previously described siRNAs and validated their efficient depletion in RPE1 cells by western blotting and loss-of-function phenotypes during cilium assembly (Fig. S4E, F,G,H) (Patzke et al., 2010; Yamazoe et al., 2020). Ciliary levels of mNG–CSPP1 and mNG–CEP104 increased in CCDC66-depleted cells relative to control cells, identifying an inhibitory role for CCDC66 in their ciliary recruitment (Fig. 5B,C,E,F). In contrast, depletion of CEP104 and CSPP1 depletions did not result in a significant change in the ciliary levels of GFP–CCDC66 (Fig. 5D,G).

Finally, we investigated the functional dependency of CCDC66, CSPP1 and CEP104 during cilium assembly and axoneme elongation. To this end, we first examined whether stable expression of mNG–CEP104 and mNG–CSPP1 restores the ciliogenesis and cilium length defects associated with CCDC66 depletion. In mNG–CEP104 or mNG–CSPP1-expressing cells, CCDC66 depletion resulted in a significant reduction in the percentage of ciliated cells (Fig. S4I,J). Strikingly, mNG–CEP104, but not mNG–CSPP1, expression compensated for the reduced cilium length defect observed in control CCDC66-depleted cells (Fig. 5H,I). Moreover, CEP104 and CSPP1 depletion reduced cilium length in RPE1::mNG-CCDC66 cells (Fig. 5J), showing that CCDC66 does not restore shorter cilium length associated with CEP104 and CSPP1 depletion. We also investigated whether CSPP1 or CEP104 co-depletion further exacerbates the cilium

Journal of Cell Science (2023) 136, jcs260327. doi:10.1242/jcs.260327

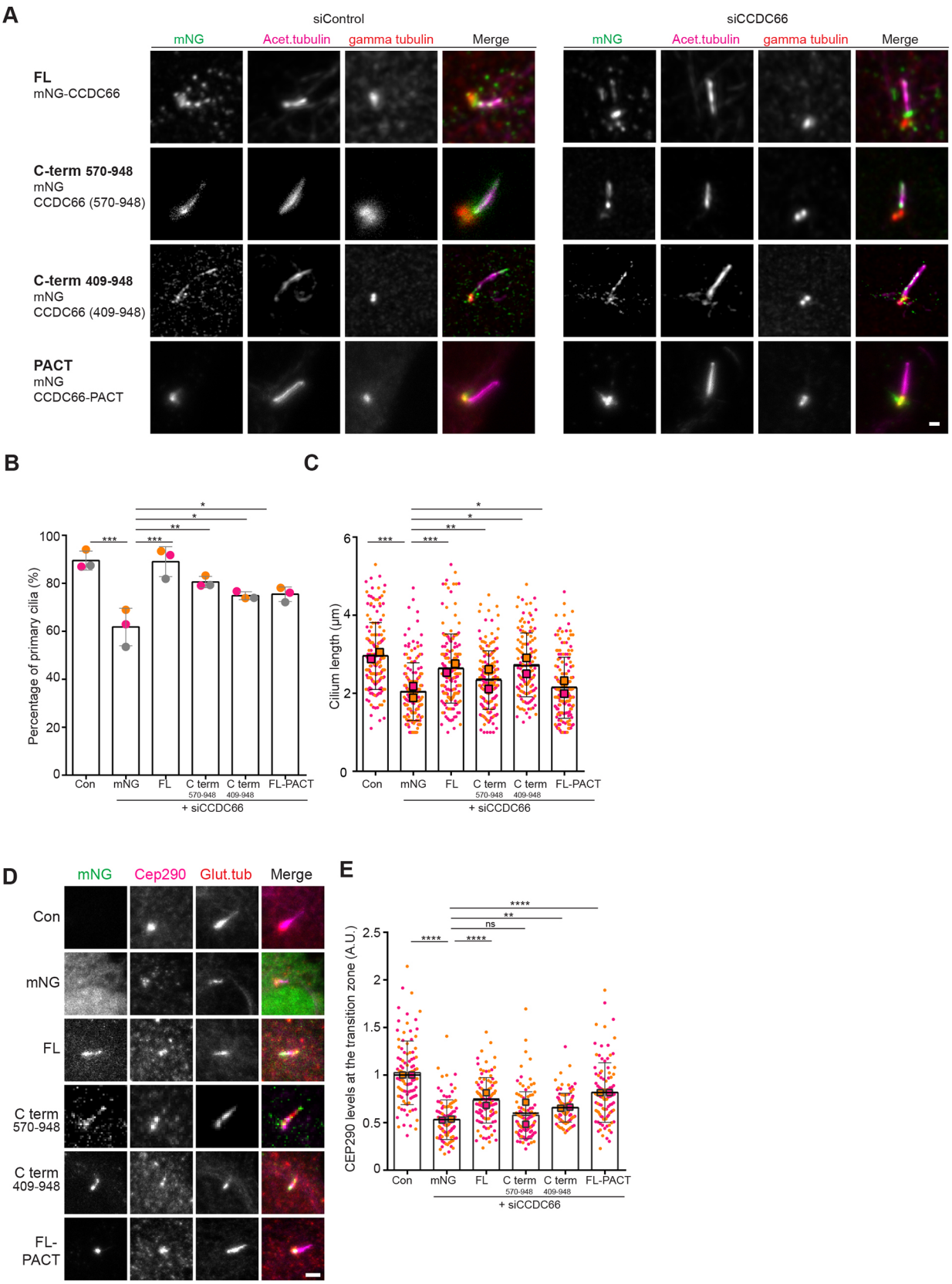

Fig. 4. See next page for legend.

length defect associated with CCDC66 depletion. In both cases, the cilia that formed in co-depleted cells were shorter relative to cells depleted for only CCDC66, indicating that these proteins are not functionally redundant (Fig. 5K,L). Taken together, our findings suggest that CCDC66 cooperates with CEP104 and CSPP1 during cilium length regulation.

Journal of Cell Science (2023) 136, jcs260327. doi:10.1242/jcs.260327

Fig. 4. Distinct CCDC66 pools cooperate during cilium and transition zone assembly. (A) Localization of C-terminal CCDC66 (570–948), (409–948) fragments and the CCDC66-PACT fusion. Control or CCDC66-depleted RPE1 cells stably expressing mNG–CCDC66 full length (FL), CCDC66 C-terminal (570–948) fragment, CCDC66 C-terminal (409–948) fragment and CCDC66-PACT fusion were serum starved for 48 h, fixed with 4% PFA and stained for acetylated tubulin and γ-tubulin. Images shown representative of two repeats. Scale bar: 1 µm. (B–E) Rescue of phenotypes. RPE1 cells with stably expressing mNG, mNG–CCDC66 full length (FL), CCDC66 C-terminal fragment (570–948) (C-term 570–948), CCDC66 C-terminal fragment (409–948) (C-term 409–948) and mNG–CCDC66-PACT fusion (FL-PACT) were transfected with CCDC66 siRNA for two rounds and serum starved for 48 h. As a control, RPE1 cells expressing mNG was transfected with control siRNA (Con). After fixation cells were stained for anti-acetylated tubulin for quantifying (B) percentage of cilium formation and (C) ciliary length, and (D) for mNG, CEP290 and polyglutamylated tubulin for quantifying CEP290 levels (E) at the transition zone. Data represent the mean±s.d. Magenta, orange and gray represent individual values from two independent experiments (100 cells/experiment for cilium formation and cilium length, 50 cells/experiment for CEP290 levels). *P<0.05; **P<0.01; ***P<0.001; ****P<0.0001; ns, not significant (one-way ANOVA with Tukey's post hoc test). A.U., arbitrary units. Scale bar: 1 µm.

CCDC66 depletion perturbs cilium content regulation and the Hedgehog pathway response

To determine whether the ciliary defects associated with CCDC66 loss affect primary cilium function, we examined the ciliary content and response to Hedgehog pathway activation of CCDC66-depleted cilia. First, we assessed the constitutive ciliary membrane proteins implicated in ciliary signaling, including the small GTPase ARL13B and ciliary G-protein-coupled receptor (GPCR) protein SSTR3. Ciliary ARL13B levels were similar between control and CCDC66-depleted cells (Fig. 6A,B). However, there was an ∼1.3-fold increase in somatostatin receptor SSTR3 ciliary level upon CCDC66 depletion (Fig. 6C,D). Next, we examined Hedgehog pathway activation in RPE1 cells transfected with control and CCDC66 siRNA. Upon stimulation of cells with Hedgehog ligands at the cilium, the GPCR SMO enters the cilium and GPR161 moves out of the cilium, which eventually leads to transcriptional activation of Hedgehog target genes (Mukhopadhyay and Rohatgi, 2014). As functional readouts for Hedgehog pathway activation, we quantified the efficiency of ciliary entry of SMO and Gli1 upregulation (Fig. 6E–J). To this end, ciliated control and CCDC66-depleted cells were treated with 100 nM Smoothened agonist (SAG) for 24 h and processed by immunofluorescence or quantitative PCR. In both control and CCDC66-depleted cells, SMO did not localize to cilia under basal conditions (Fig. 6E). Upon SAG stimulation, the ciliary level of SMO increased ∼3-fold in control cells and ∼2.3-fold in CCDC66-depleted cells (Fig. 6E,F). This significant reduction in ciliary SMO enrichment shows that CCDC66 loss interferes with its SAG-induced ciliary accumulation. Additionally, we compared the ciliary distribution and levels of SMO upon SAG treatment. Although the fraction of cells with 'tip' localization of SMO was comparable in control and CCDC66-depleted cells, there was a significant reduction in its levels at the ciliary tip upon CCDC66 depletion (Fig. 6G–I). Finally, we examined the downstream consequences of these alterations by quantifying Gli1 transcriptional upregulation in SAG-treated cells. In contrast to control cells, CCDC66-depleted cells failed to upregulate Gli1 in response to SAG treatment (Fig. 6J). Collectively, these findings demonstrate that CCDC66 is required for the formation of Hedgehog-competent cilia.

DISCUSSION

CCDC66 is a MAP that localizes to the centriolar satellites, the centrosome and the primary cilium and is linked in ciliopathies affecting retina and brain. The results of our study reveal two specific functions of CCDC66 at the primary cilium. First, it is required for assembling the primary cilium with high efficiency and in the right composition. In particular, it functions directly or indirectly during Hedgehog pathway activation. It mediates these functions in part by regulating transition zone assembly and basal body recruitment of the IFT-B complex. Second, CCDC66 interacts with the ciliopathy proteins CEP104 and CSPP1 and controls axonemal elongation. The results of our study have important implications for uncovering the mechanisms that underlie the structural and functional complexities of the primary cilium as well as pathogenesis of CCDC66-linked ciliopathies.

The distinct localization profiles of CCDC66 full-length and truncation constructs and visualization of CCDC66 dynamics during cilium biogenesis allowed us to address important questions regarding the significance of functional and dynamic compartmentalization within the centrosome and cilium complex. For example, primary cilium assembly and disassembly dynamics have so far been studied by monitoring dynamic behavior of ciliary membrane proteins (Jewett et al., 2021; Lu et al., 2015; Quanlong et al., 2021; Westlake et al., 2011). Our analysis of the localization dynamics of CCDC66 during ciliogenesis is the first report of the kinetics of the ciliary axoneme in mammalian cells. Another key finding of our study is that we identified differences in CCDC66 interaction partners at different cellular locations and defined the contribution of different CCDC66 domains to cilium biogenesis. Immunoprecipitation experiments between different CCDC66 truncations and CSPP1, CEP104, PCM1 and CEP290 identified an important role for the conserved 'CCDC66 domain' in mediating these interactions. Comparative analysis of the phenotypic rescue results in cells expressing different CCDC66 truncations that contained or lacked the 'CCDC66 domain' showed that these interactions are required for CCDC66 functions during basal body targeting of CEP290 and cilium length regulation. Although the expression of the CCDC66 fragment that binds to microtubules partially rescued the cilium formation defect upon CCDC66 depletion, affinity to microtubules and centrosomal and/or ciliary proteins, such as CEP104 and CSPP1, were required for its functions during cilium length regulation. Taken together, our results are suggestive of different mechanisms by which CCDC66 mediates its functions at the centriolar satellites versus the primary cilium.

Formation of signaling-competent cilia is a multistep process that requires nucleation of basal body-templated axonemal microtubules and their elongation and maintenance at a steady-state length. Our findings provide important insight into how the microtubule-based core of the cilium is assembled and maintained by the coordinated activity of MAPs and ciliary signaling and transport proteins. We showed that CCDC66 binds to microtubules, localizes to the axoneme and the cilium tip and interacts with axonemal and tip proteins CEP104 and CSPP1. CEP104 contains the evolutionarily conserved tubulin-binding TOG domains (Farmer and Zanic, 2021). Given the reported functions of TOG-array proteins in microtubule dynamics, CEP104 has been proposed to regulate polymerization of axonemal microtubules (Das et al., 2015; Yamazoe et al., 2020). The cilium length defect of CCDC66-depleted cells is compensated for by expression of mNG–CEP104, suggesting that CCDC66 might regulate CEP104-mediated axonemal microtubule polymerization. This rescue can be explained by increased

Journal of Cell Science (2023) 136, jcs260327. doi:10.1242/jcs.260327

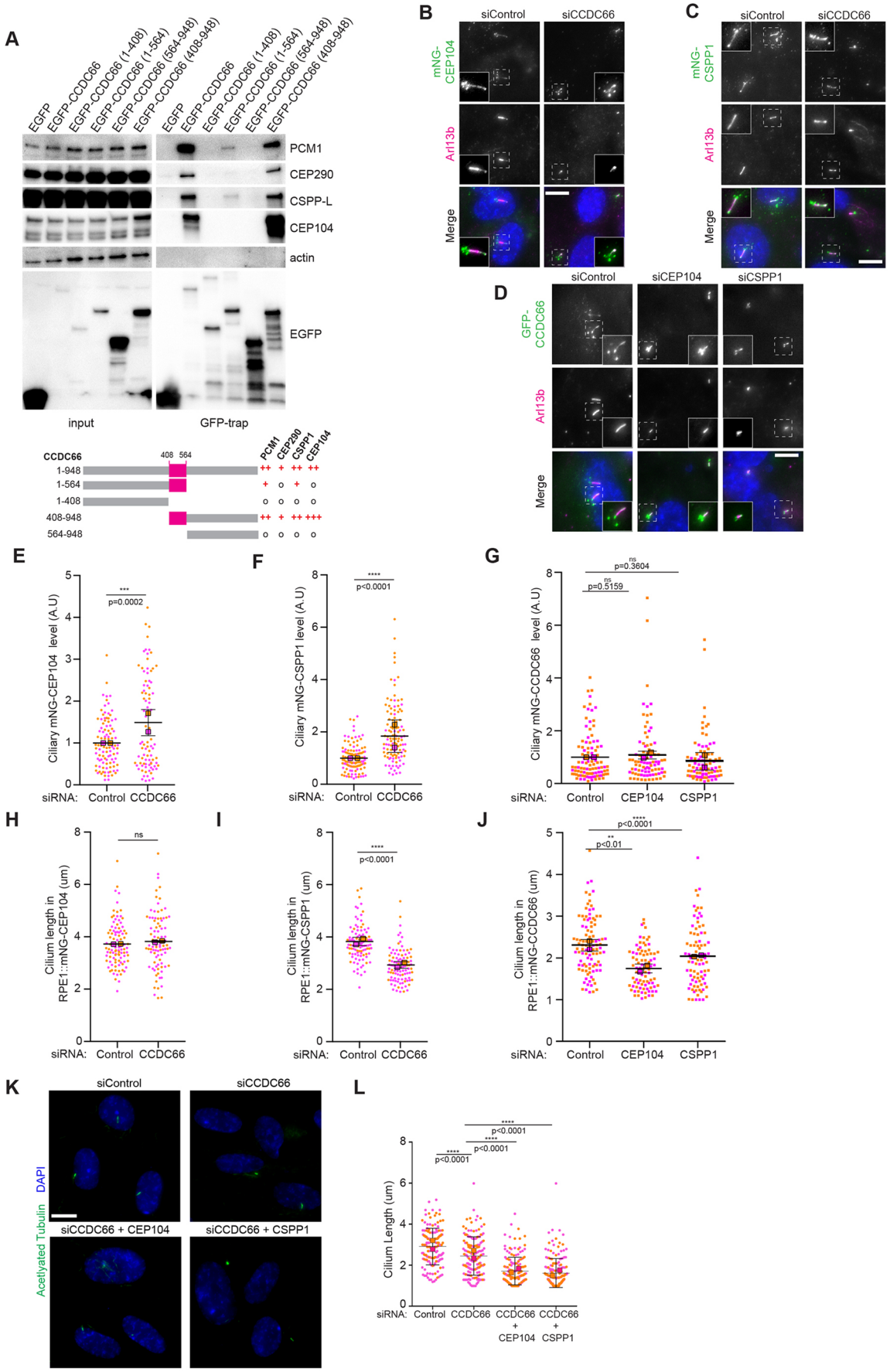

Fig. 5. See next page for legend.

Journal of Cell Science (2023) 136, jcs260327. doi:10.1242/jcs.260327

Fig. 5. CCDC66 forms a functional complex with CSPP1 and CEP104. (A) CCDC66 interacts with CSPP1 and CEP104. HEK293T cells were transfected with EGFP, EGFP–CCDC66 full length, and 1–408, 1–564, 564–948 and 408–948 constructs, and immunoprecipitated with GFP Trap beads. Input (5%) and pellet fractions were immunoblotted for GFP, PCM1, CEP290, CSPP1, CEP104 and actin as a loading control. The scheme underneath summarizes the CCDC66 N- and C-terminal constructs and their interactions with indicated proteins (o, no interaction; +, weak interaction; ++, moderate interaction; +++, strong interaction). (B,C,E,F,H,I) CCDC66 negatively regulates ciliary CSPP1 and CEP104 level. (B) RPE1::mNG–CEP104 or (C) RPE1::mNG–CSPP1 cells were transfected with two rounds of control or CCDC66 siRNA and serum starved for 48 h. Following fixation, cells were stained for mNG and ARL13B, and with DAPI for visualization of DNA. (E) Ciliary mNG–CEP104 or (F) mNG–CSPP1 signal was quantified by measuring the mNG signal intensity using the area covered by ARL13B signal, subtracting the background signal, and dividing it by the length of the cilia. Cilium lengths (H,I) were measured and plotted. Data represent the mean±s.d. Magenta and orange represent individual values from two independent experiments (50 cilia/experiment). **P*<0.05; ***P*<0.01; ****P*<0.001; *****P*<0.0001; ns, not significant (unpaired two-tailed *t*-test). A.U., arbitrary units. Scale bars: 10 µm. (D,G,J) Regulation of CCDC66 ciliary targeting by CEP104 and CSPP1. RPE1::mNG–CCDC66 cells were transfected with two rounds of control, CEP104 or CSPP1 siRNA and serum starved for 48 h. (D) Following fixation, cells were stained for mNG and ARL13B, and with DAPI for visualization of DNA. (G) Ciliary mNG–CCDC66 signal was quantified by measuring the mNG signal intensity using the area covered by ARL13B signal and dividing it by the length of the cilia. Cilium lengths (J) were plotted. Data represent the mean±s.d. Magenta and orange represent individual values from two independent experiments. (50 cilia/experiment). **P*<0.05; ***P*<0.01, ****P*<0.001; *****P*<0.0001; ns, not significant (unpaired two-tailed *t*-test). Scale bar: 10 µm. (K,L) Co-depletions of CEP104 or CSPP1 with CCDC66 results in shorter cilia than CCDC66 depletion. (K) RPE1 cells were transfected with two rounds of control, CCDC66, CCDC66 along with CEP104 and CCDC66 along with CSPP1 siRNA and fixed at 48 h serum starvation. Following fixation, cells were stained for acetlyated tubulin and with DAPI. (L) Cilium length is plotted. Magenta and orange represent individual values from two independent experiments. Error bars represent±s.d. Square boxes represents the mean value of each experiment for each group. (50 cilia/experiment). **P*<0.05; ***P*<0.01; ****P*<0.001; *****P*<0.0001; ns, not significant (one-way ANOVA with Tukey's post hoc test). Scale bar: 10 µm.

CEP104 levels in CCDC66-depleted cells because the TOG domain of CEP104 has been shown to promote microtubule polymerization *in vitro* and rescue the cilium length defect associated with CEP104-depletion (Yamazoe et al., 2020). Future studies aiming to uncover how CCDC66 regulates microtubule polymerization and dynamics *in vitro* are required to fully explain the CCDC66 mode of action at the axoneme.

Centriolar satellites have emerged as regulators of cilium assembly and composition in part via centrosomal and ciliary targeting of proteins implicated in these processes (Aydin et al., 2020; Gheiratmand et al., 2019; Quarantotti et al., 2019). Characterization of CCDC66 dynamics during ciliogenesis revealed that its centriolar satellite pool of CCDC66 started disappearing as its ciliary pool appeared. Although this result supports the sequestration and active transport functions of satellites, whether the source of ciliary CCDC66 is newly synthesized protein or its centriolar satellite pools is not known. Our findings on the nature of the CEP290–CCDC66 relationship also provides insight into how satellites regulate primary cilium biogenesis and function. We show that CCDC66 is required for transition zone assembly via regulating ciliary targeting of CEP290. Taking into account previous work that revealed a critical role for the satellite pool of CEP290 during transition zone assembly, we propose the following model for the functional significance of the CCDC66–CEP290 interaction (Kobayashi et al., 2014; Tu et al., 2018): CCDC66 maintains the satellite pool of CEP290 by tethering it to PCM1, and satellites regulate basal body targeting of CEP290 by sequestration or active transport. This model is supported by two lines of evidence. First, we found an inverse correlation of the number and integrity of satellite granules with the growth of primary cilium. Second, tethering CCDC66 to the centrosome via its PACT fusion was accompanied by lack of its satellite pool and restoration of CEP290 levels at the transition zone in CCDC66-depleted cells. In addition to CEP290, the centriolar satellite pool of CCDC66 might also regulate cilium content via ciliary targeting of the transport complexes.

We identified the *in vivo* proximity interactome of CCDC66 in ciliated cells. Although the resulting map provided insight into ciliary functions and mechanisms of CCDC66, we note that it has low overlap with the published proximity interactomes of the cilium generated by APEX fusions of ciliary targeting sequences of membrane proteins (Kohli et al., 2017; May et al., 2021; Mick et al., 2015). There are two possible explanations for the low overlap. First, CCDC66 localizes to the centriolar satellites, basal body and primary cilium in ciliated cells. Therefore, its ciliary interactions might be of lower abundance than those with its other cellular pools. Second, CCDC66 might mediate its structural functions at the axoneme by forming a stable complex, which would limit its interactions with other ciliary proteins. This is supported by previous FRAP data, which revealed that ciliary pools of CCDC66 and its interactor CSPP1 are immobile (Conkar et al., 2019; Frikstad et al., 2019). Future studies that define the functional relationship of CCDC66 to its proximity interactors at the cilia are required to uncover the full extent of its mechanisms.

In summary, our findings identify a complex molecular and functional relationship between the different compartments of the centrosome and cilium complex and provide directions for future studies on the molecular basis of differential complex formation and intricate interplay of ciliopathy proteins during cilium biogenesis and function. Future studies on elucidating the functions of CCDC66 in different cell types and tissues will contribute to our understanding of how its deregulation is linked to ciliopathies.

MATERIALS AND METHODS

Cell culture, transfection and lentiviral transduction

Human embryonic kidney (HEK293T, ATCC, CRL-3216) cells were cultured with Dulbecco's modified Eagle's medium (DMEM; Pan Biotech) supplemented with 10% fetal bovine serum (FBS; Life Technologies) and 1% penicillin-streptomycin (Gibco). Human telomerase immortalized retinal pigment epithelium cells (hTERT-RPE, ATCC, CRL-4000) and mouse kidney medulla collecting duct cells IMCD3:Flip-In cells (gift from Max Nachury, UCSF, CA, USA) were cultured with DMEM/F12 50/50 medium (Pan Biotech), supplemented with 10% FBS and 1% penicillin-streptomycin. RPE1::mNG-CEP104 and RPE1::mNG-CSPP1 cell lines were described previously (Frikstad et al., 2019). All cell lines were tested for mycoplasma with the MycoAlert Mycoplasma Detection Kit (Lonza). RPE1 cells were transfected using Lipofectamine LTX (Thermo Scientific). HEK293T cells were transfected with the indicated plasmids using 1 µg/µl polyethylenimine, MW 25 kDa (PEI, Sigma-Aldrich).

Lentivirus were generated using pcDH-mNG-CCDC66, pcDH-mNG-CCDC66 (409-948), pcDH-mNG-CCDC66 (570-948), pcDH-mNG-CCDC66-PACT and pCDH-EF1-mNeonGreen-T2A-Puro and pLVPT2-mScarlet-Arl13b plasmids (see below) as transfer vectors. RPE1 cells were transduced with the indicated lentivirus and selected with 6 µg/ml puromycin for 4–6 days until all the control cells died. IMCD3 cells stably expressing FLAG-miniTurbo and FLAG-miniTurbo-CCDC66 were generated using previously described protocols (Odabasi et al., 2019). Briefly, cells were co-transfected with pcDNA5.1-FRT/TO expression vectors and pOG44 (Thermo Fisher Scientific) at a ratio of 1:7 using

Journal of Cell Science (2023) 136, jcs260327. doi:10.1242/jcs.260327

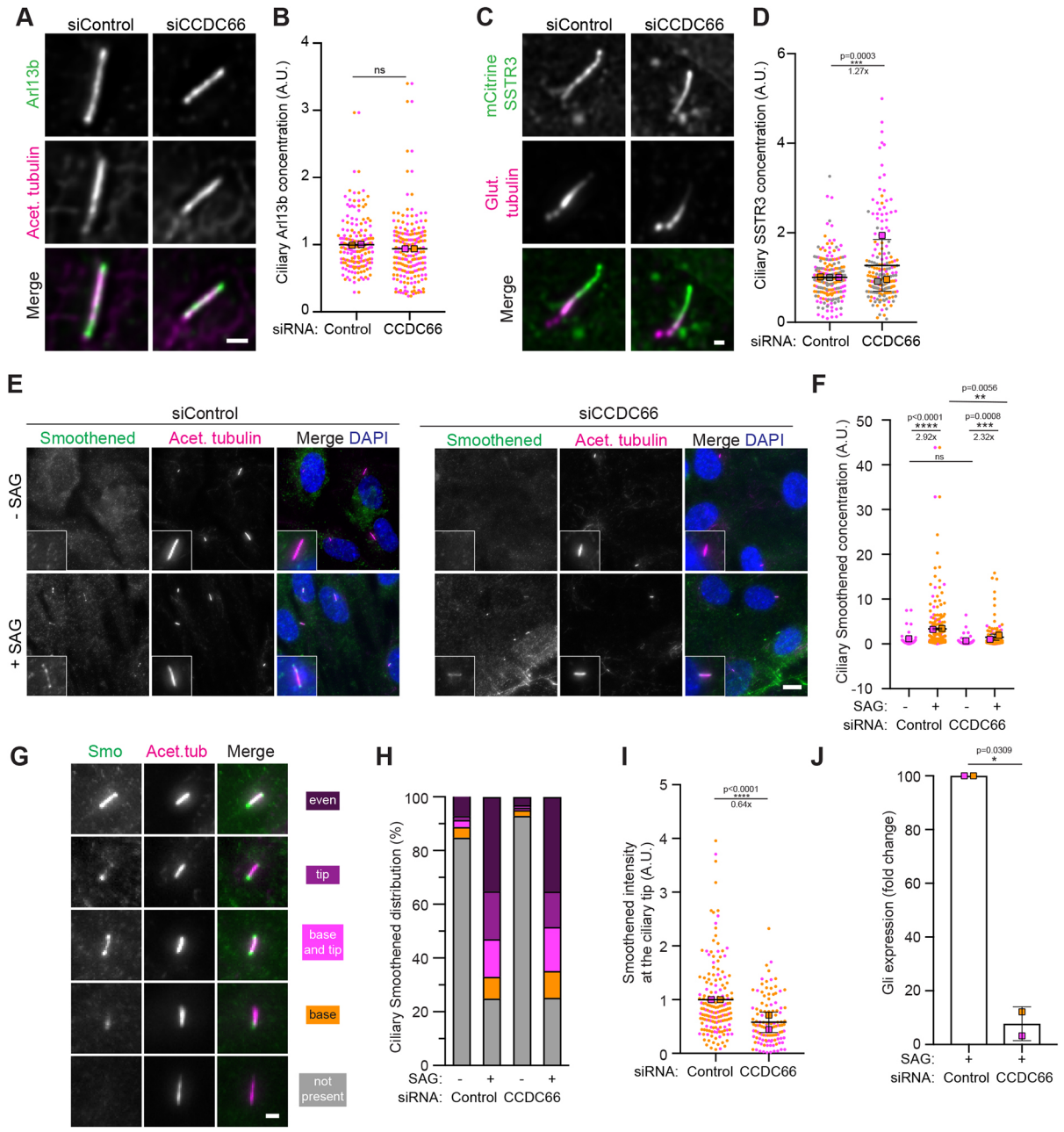

Fig. 6. CCDC66 impairs Hedgehog pathway activation. (A,B) CCDC66 is not required for ciliary ARL13B recruitment. RPE1 cells were transfected with two rounds of control or CCDC66 siRNA and serum starved for 48 h. Cells were fixed and stained for ARL13B and acetylated tubulin. Ciliary ARL13B levels were quantified by measuring the ARL13B intensity at cilia, subtracting the background signal, multiplied by the signal area, and dividing by the cilium length. Data represent the mean±s.d. Magenta and orange represent individual values from two independent experiments (50 cilia/experiment). ns, not significant (unpaired two-tailed *t*-test). A.U., arbitrary units. Scale bar: 1 µm. (C,D) CCDC66 depletion causes ciliary SSTR3 accumulation. RPE1::mCitrine–SSTR3 cells were transfected with two rounds of control or CCDC66 siRNA and serum starved for 48 h. Cells were fixed with 4% PFA and stained for polyglutamylated tubulin. Ciliary mCitrine–SSTR3 levels were quantified by measuring the SSTR3 intensity at cilia, subtracting the background signal, multiplied by the signal area, and dividing by the cilium length. Data represent the mean±s.d. Magenta and orange represent individual values from two independent experiments (50 cilia/experiment). ***P<0.001 (unpaired two-tailed *t*-test). Scale bar: 1 µm. (E–I) CCDC66 depletion compromises ciliary recruitment and distribution of SMO. RPE1 cells were transfected with two rounds of control or CCDC66 siRNA and serum starved for 24 h and incubated with (0.01%) DMSO or 100 nM SAG for the subsequent 24 h. (E) Cells were fixed and stained for Smoothened and acetylated tubulin, and with DAPI. Hedgehog activation was assessed by (F) determining ciliary Smoothened levels, quantified by measuring the SMO intensity at cilia, (G,H) assessment of the localization of Smoothened in the absence and presence of SAG, and determining (I) the ciliary tip levels of Smoothened in SAG-treated cells. There is no significant statistical difference (one-way ANOVA with Tukey's post hoc test) between categories shown in the graph (H). Data represent the mean±s.d. Magenta and orange represent individual values from two independent experiments (50 cilia/experiment). *P<0.05; **P<0.01; ***P<0.001; ****P<0.0001; ns, not significant [one-way ANOVA with Tukey's post hoc test (F), unpaired two-tailed *t*-test (I)]. Scale bars: 10 µm (C); 2 µm (E). (J) CCDC66 depletion affects GLI1 upregulation as a response of Hedgehog signaling activation. Upregulation of GLI1 expression in control and CCDC66-depleted cells treated with (0.01%) DMSO or 100 mM SAG. GLI1 mRNA levels were quantified by qPCR before SAG treatment and 24 h after SAG treatment, and its fold change is normalized to control cells (=100). Results shown are the mean±s.d. of two independent experiments. *P<0.05 (unpaired two-tailed *t*-test).

Lipofectamine LTX, selected with 300 µg/ml hygromycin B and individual colonies were picked and validated by immunofluorescence.

For cilium assembly experiments, cells were washed twice with PBS and incubated with DMEM/F12 50/50 supplemented with 0.5% FBS and 1% penicillin-streptomycin for the indicated times. For cilium disassembly experiments, cells that were incubated with 0.5% FBS for 48 h were washed twice with PBS and incubated with DMEM/F12 50/50 supplemented with 10% FBS and 1% penicillin-streptomycin for the indicated times. For Hedgehog pathway activation, cells were incubated with 100 nM Smoothened agonist (SAG, EMD Millipore) or DMSO for 24 h following 24 h of serum starvation.

Plasmids and siRNAs transfections

pDEST-GFP-CCDC66, pDEST-GFP-CCDC66^{RR} and pDEST-Flag-CCDC66 plasmids were previously described (Conkar et al., 2017). Full-length CCDC66 was cloned into pcDNA5.1-FRT/TO-FLAG-miniTurbo pOG44 (Thermo Fisher Scientific) vector to generate IMCD3 stable lines using the Flip-In approach. Full-length CCDC66, CCDC66 (570–948) and CCDC66-PACT were cloned into pCDH-EF1-mNeonGreen-T2A-Puro lentiviral expression plasmid (Gurkaslar et al., 2020). siRNA resistant mNeonGreen-CCDC66 was amplified from siRNA resistant GFP-CCDC66^{RR} plasmid and cloned into pCDH-EF1-mNeonGreen-T2A-Puro plasmid (Gurkaslar et al., 2020). CCDC66 was depleted using an siRNA with the sequence 5′-CAGTGTAATCAGTTCACAAtt-3′ (Thermo Fisher Scientific). Silencer Select Negative Control No. 1 (Thermo Scientific) was used as a control. CSPP1 and CEP104 were depleted by RNAi using previously described siRNAs (Patzke et al., 2010; Yamazoe et al., 2020). Cells were seeded onto coverslips at 70% confluency and transfected with 50 nM of siRNA in two sequential transfections using Lipofectamine RNAiMAX (Life Technologies) in OPTI-MEM (Life Technologies) according to the manufacturer's instructions. Depletion of proteins was confirmed at 48 h or 72 h after transfection by immunofluorescence and immunoblotting.

Immunofluorescence and antibodies

Cells were grown on coverslips, washed twice with PBS and fixed with either ice-cold methanol at −20°C for 10 min or 4% PFA in cytoskeletal buffer (10 mM PIPES, 3 mM $MgCl_2$, 100 mM NaCl, 300 mM sucrose, pH 6.9) supplemented with 5 mM EGTA and 0.1% Triton X for 15 min at 37°C. After washing twice with PBS, cells were blocked with 3% BSA in PBS plus 0.1% Triton X-100 and incubated with primary antibodies in blocking solution for 1 h at room temperature. Cells were washed three times with PBS and incubated with secondary antibodies and DAPI (Thermo Fisher Scientific) at 1:2000 for 45 min at room temperature. Following three washes with PBS, cells were mounted using Mowiol mounting medium containing N-propyl gallate (Sigma-Aldrich).

The detergent incubation protocol to assess axonemal association of CCDC66 is adapted from Nachury et al. (2007). Briefly, cells were washed twice with PHEM buffer (60 mM PIPES, 25 mM HEPES, 10 mM EGTA, 4 mM $MgSO_4$, pH 7.0) and incubated with either PHEM or PHEM plus 0.5% Triton-X for 30 s. After incubation, they were fixed with 4% PFA at 37°C and processed for microscopic analysis. Primary antibodies used for immunofluorescence were rabbit anti-IFT88 (13967-1-AP, Proteintech) at 1:50, rabbit anti-IFT81 (11744-1-AP, Proteintech) at 1:50, rabbit anti-CP110 (A301-344A, Betyl) at 1:500, mouse anti-PCM1 at 1:1000 (sc-398365, Santa Cruz Biotechnology), rabbit anti-CEP290 (800 338 9579, Betyl) at 1:500, mouse anti-BBS1 (sc-365138, Santa Cruz Biotechnology) at 1:50, mouse anti-BBS2 (sc-365355, Santa Cruz Biotechnology) at 1:50, mouse anti-BBS3 (sc-390021, Santa Cruz Biotechnology) at 1:50, mouse anti-CEP164 (sc-515403, Santa Cruz Biotechnology) at 1:1000, mouse anti-Smoothened (sc-166685, Santa Cruz Biotechnology) at 1:50, mouse anti-polyglutamylated tubulin (AG-20B-0020, clone GT335, Adipogen), mouse anti-γ-tubulin (T5326, clone GTU-88, Sigma) at 1:1000, mouse anti-acetylated tubulin (clone 6-11B, 32270, Thermo Fisher Scientific) at 1:10,000, rabbit anti-ARL13B (17711-1-AP, Proteintech) at 1:50, mouse anti-ARL13B (75-287, NIH Neuromab) at 1:100, mouse anti-GFP (3E6, Invitrogen) at 1:750. Rabbit anti-GFP and rabbit anti-PCM1 antibodies were generated and used for immunofluorescence as previously described (Conkar et al., 2017). Anti-CCDC66 antibody was generated by immunizing rats (Koc University, Animal Facility) with His-MBP-tagged mouse CCDC66 (clone 30626499) comprising amino acids 1–756 purified from Hi5 insect cells. The antibody was affinity purified against His–MBP–mCCDC66 (a.a. 1–756) and used at 0.5 µg/ml for immunofluorescence. Secondary antibodies used for immunofluorescence experiments were Alexa Fluor 488-, 568- or 633-coupled (Life Technologies) and they were used at 1:2000. Secondary antibodies used for western blotting experiments were IRDye 680-and IRDye 800-coupled and were used at 1:15,000 (LI-COR Biosciences), peroxidase AffiniPure donkey anti-mouse-IgG (H+L) (715-035-150, Jackson ImmunoResearch) and peroxidase AffiniPure goat anti-rabbit-IgG (H+L) (111-035-144, Jackson ImmunoResearch) were used for western blotting.

Microscopy and image analysis

Time lapse live imaging was performed in an incubation chamber on a Leica SP8 confocal microscope with an HC PL APO CS2 63x 1.4 NA oil objective. For imaging CCDC66 localization dynamics during cilium assembly, cells were incubated with 0.5% FBS in DMEM/F12 after two rounds of siRNA transfection and imaged overnight at every 12 min per frame in 512×512 pixel format. For cilium disassembly, cells that were transfected with siRNA, serum starved for 2 days. Following serum stimulation, cilium disassembly was imaged overnight at every 12 min in 512×512 pixel format. For protein level and localization percentage quantifications, images were acquired with Leica DMi8 fluorescent microscope with a stack size of 8 µm and step size of 0.3 µm in 1024×1024 format using an HC PL APO CS2 63×1.4 NA oil objective. Higher resolution images were taken by using an HC PL APO CS2 63×1.4 NA oil objective with Leica SP8 confocal microscope. For super-resolution imaging of subcentrosomal GFP–CCDC66 localization, images were acquired using Elyra 7 with Lattice SIM² (Zeiss). All data were captured using Zeiss Objective Plan-Apochromat 63×/1.4 Oil DIC M27, 568 nm and 488 nm laser illumination, and standard excitation and emission filter sets. Sections were acquired at 0.110 µm *z*-steps. Images were processed using ImageJ (National Institutes of Health, Bethesda, MD).

Quantitative immunofluorescence of centrosomal and ciliary levels of proteins was performed by acquiring a *z*-stack of cells using identical gain and exposure settings, determined by adjusting settings based on the fluorescence signal in the control cells. The *z*-stacks were used to assemble maximum-intensity projections. The centrosome regions in these images were defined by centrosomal marker staining for each cell, and the total pixel intensity of a circular 2.5 µm^2 area centered on the centrosome in each cell was measured using ImageJ and defined as the centrosomal intensity. For transition zone quantification, a 2.5 µm^2 area above basal body was measured. The basal body was defined as the area showing glutamylated tubulin signal. The ciliary regions in these images were defined by the ARL13B or acetylated tubulin signal for each cell. For the basal body acetylated tubulin levels, a 2.2 µm^2 region of interest (ROI) was drawn and three random areas were quantified using this ROI. The background intensity was subtracted from their average. Background subtraction was performed by quantifying fluorescence intensity of a region of equal dimensions in the area neighboring the centrosome or cilium. Ciliary protein levels were determined by dividing fluorescence signal of the protein to the cilium length, which was quantified using ARL13B or acetylated tubulin staining. Centrosomal and ciliary protein levels were normalized relative to the mean of control group (=1). Line analysis was performed by drawing a line covering the basal body and ciliary signal of GFP–CCDC66 signal and the marker. Each protein signal was normalized to average intensity of the its own signal, and plotted. Primary cilium formation was assessed by counting the total number of cells and the number of cells with primary cilia, as detected by ARL13B or acetylated tubulin staining and DAPI staining. Localization percentage quantifications were performed by counting the number of cilia using a ciliary marker, such as acetylated tubulin or ARL13B, and the number of cilia with the desired protein signal and calculating the percentage of positivity for the corresponding protein.

To assess Hedgehog pathway activation, the ciliary Smoothened level was measured by determining the background subtracted ciliary

Smoothened signal divided by the ciliary length. Ciliary tip levels of Smoothened was quantified by measuring Smoothened signal within a 0.5 μm^2 ROI above the acetylated tubulin marker and subtracting it from the background signal. Ciliary Smoothened distribution categories were determined according to the observed Smoothened distribution patterns. All data acquisition was done by a researcher who was not aware of the experimental conditions.

For analysis of live imaging movies, the frame in which the cilium had started to form was determined by the bulging of CCDC66 or Smoothened signal from the basal body. Quantification of ectocytosis, breakage (scission) and ripping off events was performed manually by inspection of each cilium. Breakage events were distinguished from ectocytosis events by the length of the ciliary piece released (ectocytosis event<0.5 µm; breakage or rip-off event>0.5 µm). All values representing levels were normalized relative to the mean of control group. (=1). Statistical significance was determined by performing an unpaired two-tailed Student's *t*-test using Prism (GraphPad, La Jolla, CA).

Cell lysis and immunoblotting

Cells were washed with PBS twice and lysed in the lysis buffer (50 mM Tris-HCl pH 7.6, 150 mM NaCl, 1% Triton X-100), tumbled at 4°C for 40 min and centrifuged at 15,000 ***g***. Protein concentration was measured with Bradford solution (Bio-Rad Laboratories, CA, USA). The resulting supernatant was added with 6× sample buffer, boiled for 10 min at 95°C. Proteins were separated by SDS-PAGE, transferred to nitrocellulose membranes (Bio-Rad Laboratories, CA, USA) and blocked with 5% milk in TBS with 1% Tween-20. Primary antibody incubation was performed at 4°C overnight or at room temperature for 2 h. Primary antibodies used for immunofluorescence were rabbit anti-CCDC66 (HPA044185, Sigma) at 1:500, rabbit anti-CEP290 (22490-1-AP, Proteintech) at 1:1000, rabbit anti-CSPP1 (11931-1-AP, Proteintech) at 1:1000, mouse anti-polyglutamylated tubulin (GT335, Adipogen, AG-20B-0020) at 1:500, mouse anti-acetylated tubulin (6-11-B, Sigma-Aldrich, T6793) at 1:500, mouse anti-α-tubulin (T9026, Sigma) at 1:5000, anti-vinculin (H-10, Santa Cruz Biotechnology, sc-25336) at 1:1000. Anti-CEP104 antibody was gift from Anna Akmanova, University of Utrecht, The Netherlands. Secondary antibodies used for western blotting experiments were IRDye 680- and IRDye 800-coupled and were used at 1:15,000 (Li-Cor Biosciences). Secondary antibody incubation was performed at room temperature for 1 h. Membranes were washed with PBS for 15 min and scanned in Li-Cor Odyssey® Infrared Imaging System software (Li-Cor Biosciences) at 169 µm. A ChemiDoc MP Imaging System (Bio-Rad Laboratories, CA, USA) was used for peroxidase coupled secondary antibodies. SuperSignal™ West Pico PLUS Chemiluminescent Substrate (Thermo Scientific), SuperSignal™ West Dura Extended Duration Substrate (Thermo Scientific), SuperSignal™ West Femto Maximum Sensitivity Substrate (Thermo Scientific) were used as chemiluminescence reagents. Quantifications of band intensities and cropping of the images were performed in ImageJ.

Biotin identification with miniTurbo and mass spectrometry analysis

IMCD3 cells stably expressing miniTurbo or miniTurbo-CCDC66 were used. For mass spectrometry analysis, each cell type was grown in 5×15 cm plates in DMEM/F12 medium supplied with 10% FBS and 1% penicillin-streptomycin. The ciliated cell populations were generated after growing cells to 100% confluency and serum starving them for 48 h in DMEM/F12 with 0% FBS. Both cell populations were incubated with 500 µM biotin for 30 min. Streptavidin pulldowns were performed as described previously. After washing twice with PBS at room temperature, cells were collected and lysed in RIPA buffer (50 mM Tris-HCl pH 8.0, 150 mM NaCl, 0.1% SDS, 0.5% sodium deoxycholate, 1% Triton X-100) freshly supplied with 1× ProBlock protease inhibitor cocktail (GoldBio), and 1 mM PMSF. Cell lysates were sonicated, and their protein concentration were determined. 2.5% of the lysate was saved as the initial sample. Lysates were centrifuged at 16,000 ***g*** for 1 h at 4°C. The pellet and 50 µl of supernatant were saved for SDS-PAGE analysis. The remaining supernatant was incubated with 200 µl Streptavidin–agarose beads (Thermo Fisher Scientific) for 16 h at 4°C. Following incubation, beads were washed twice with RIPA buffer, once with 1 M KCl, once with 0.1 M Na_2CO_3, once with 2 M urea in 10 mM Tris-HCl pH 8.0, and finally twice with RIPA buffer. For mass spectrometry analysis, beads were resuspended in 100 µl of 50 mM ammonium bicarbonate and performed at KUPAM proteomics facility as previously described (Gurkaslar et al., 2020). For miniTurbo experiment, data presented in the table or network format in Fig. S4 and Table S1, data were derived from two biological replicates and two technical replicates.

For mass spectrometry analysis, Normalized Spectral Abundance Factor (NSAF) values were generated for each protein by dividing each Peptide Spectrum Match (PSM) value by the total PSM count in that dataset. Datasets were filtered as follows. First, proteins that were present only in the control dataset and in only one of the technical datasets were removed. NSAF values in the CCDC66 dataset were divided by the corresponding NSAF value from the control dataset to calculate an enrichment score for filtering proteins that were more abundant in the ciliated datasets. For proteins present in both experimental replicas, the average of enrichment score was calculated. Proteins with enrichment score <2 were removed. Next, the remaining proteins were submitted to CRAPome (https://reprint-apms.org), which is a contaminant repository for mass spectrometry data collected form affinity purification experiments and a list with contaminancy percentage (%) was calculated (Mellacheruvu et al., 2013). Proteins with contaminancy percentage more than 25% were considered as a contaminant and removed. This cut-off value was chosen depending on whether there was a known interaction partner of CCDC66 within the range of that value. Finally, proteins were listed according to their NSAF values and the interactome map was generated using Cytoscape (Shannon et al., 2003).

RNA isolation, cDNA synthesis and qPCR

Total RNA was isolated from control and IMCD PCM1 KO cells before SAG treatment and 24 h after SAG treatment using NucleoSpin RNA kit (Macherey-Nagel) according to the manufacturer's protocol. Quantity and purity of RNA were determined by measuring the optical density at 260 and 280 nm. Single-strand cDNA synthesis was carried out with 1 mg of total RNA using SCRIPT Reverse Transcriptase (Jena Bioscience). qPCR analysis of Gli1 was performed with primers 5′-CCAACTCCACAGGCATACAGGAT-3′ and 5′-CACAGATTCAGGCT-CACGCTTC-3′ using GoTaq® qPCR Master Mix (Promega).

Statistical tests

Graphpad Prism 7 was used for applying statistical tests and generating graphs. Two experimental groups were compared using unpaired two-tailed Student's *t*-test, whereas experiments involving more than two experimental groups were analyzed using one- or two-way ANOVA with Tukey's post hoc test. Number of analyzed cells or experimental replicas for each condition are indicated at figure legend. Error bars indicate standard deviation (s.d.) and significancy levels are denoted as ns>0.05, *P<0.05, **P<0.01, ***P<0.001, ****P<0.0001.

Acknowledgements

We acknowledge the Firat-Karalar lab members for insightful discussions regarding this work.

Competing interests

The authors declare no competing or financial interests.

Author contributions

Conceptualization: E.O., D.C., J.D., S.P., E.N.F.-K.; Methodology: E.O., D.C., E.N.F.-K.; Validation: E.O., D.C.; Formal analysis: E.O., D.C.; Investigation: E.N.F.-K.; Data curation: E.O., D.C., J.D., U.B., K.-A.M.F., S.P.; Writing - original draft: E.O., D.C., E.N.F.-K.; Writing - review & editing: E.N.F.-K.; Visualization: E.O., D.C.; Supervision: E.N.F.-K.; Project administration: E.N.F.-K.; Funding acquisition: J.D., E.N.F.-K.

Funding

This project has received funding from the European Union's Horizon 2020 research and innovation program under the Marie Sklodowska-Curie grant agreement no. 896644 awarded to J.D., and the European Research Council Starting grant agreement no. 679140 to E.N.F.-K. This work was also supported by an European

Molecular Biology Organization (EMBO) Installation Grant 3622 and Young Investigator Award to E.N.F.-K., Scientific and Technological Research Council of Turkey (TUBITAK) Directorate of Science Fellowships and Grant Programmes (BIDEB) 120C148 grant to E.N.F.-K. and Norwegian Cancer Society (Kreftforeningen), Career Development Grant 6839316 to S.P.

Data availability

All relevant data can be found within the article and its supplementary information.

First Person

This article has an associated First Person interview with the first author of the paper.

Peer review history

The peer review history is available online at https://journals.biologists.com/jcs/lookup/doi/10.1242/jcs.260327.reviewer-comments.pdf

References

Al-Jassar, C., Andreeva, A., Barnabas, D. D., McLaughlin, S. H., Johnson, C. M., Yu, M. and van Breugel, M. (2017). The ciliopathy-associated Cep104 protein interacts with tubulin and Nek1 kinase. *Structure* **25**, 146-156. doi:10.1016/j.str.2016.11.014

Aydin, O. Z., Taflan, S. O., Gurkaslar, C. and Firat-Karalar, E. N. (2020). Acute inhibition of centriolar satellite function and positioning reveals their functions at the primary cilium. *PLoS Biol.* **18**, e3000679. doi:10.1371/journal.pbio.3000679

Batman, U., Deretic, J. and Firat-Karalar, E. N. (2022). The ciliopathy protein CCDC66 controls mitotic progression and cytokinesis by promoting microtubule nucleation and organization. *PLoS Biol.* **20**, e3001708. doi:10.1371/journal.pbio.3001708

Bedoni, N., Haer-Wigman, L., Vaclavik, V., Tran, V. H., Farinelli, P., Balzano, S., Royer-Bertrand, B., El-Asrag, M. E., Bonny, O., Ikonomidis, C. et al. (2016). Mutations in the polyglutamylase gene TTLL5, expressed in photoreceptor cells and spermatozoa, are associated with cone-rod degeneration and reduced male fertility. *Hum. Mol. Genet.* **25**, 4546-4555. doi:10.1093/hmg/ddw282

Betleja, E. and Cole, D. G. (2010). Ciliary trafficking: CEP290 guards a gated community. *Curr. Biol.* **20**, R928-R931. doi:10.1016/j.cub.2010.09.058

Blacque, O. E. and Sanders, A. A. (2014). Compartments within a compartment: what C. elegans can tell us about ciliary subdomain composition, biogenesis, function, and disease. *Organogenesis* **10**, 126-137. doi:10.4161/org.28830

Bodakuntla, S., Jijumon, A. S., Villablanca, C., Gonzalez-Billault, C. and Janke, C. (2019). Microtubule-associated proteins: structuring the cytoskeleton. *Trends Cell Biol.* **29**, 804-819. doi:10.1016/j.tcb.2019.07.004

Braun, D. A. and Hildebrandt, F. (2017). Ciliopathies. *Cold Spring Harb. Perspect. Biol.* **9**, a028191. doi:10.1101/cshperspect.a028191

Breslow, D. K. and Holland, A. J. (2019). Mechanism and regulation of centriole and cilium biogenesis. *Annu. Rev. Biochem.* **88**, 691-724. doi:10.1146/annurev-biochem-013118-111153

Broekhuis, J. R., Leong, W. Y. and Jansen, G. (2013). Regulation of cilium length and intraflagellar transport. *Int. Rev. Cell Mol. Biol.* **303**, 101-138. doi:10.1016/B978-0-12-407697-6.00003-9

Čajánek, L. and Nigg, E. A. (2014). Cep164 triggers ciliogenesis by recruiting Tau tubulin kinase 2 to the mother centriole. *Proc. Natl. Acad. Sci. USA* **111**, E2841-E2850. doi:10.1073/pnas.1401777111

Chien, A., Shih, S. M., Bower, R., Tritschler, D., Porter, M. E. and Yildiz, A. (2017). Dynamics of the IFT machinery at the ciliary tip. *eLife* **6**, e28606. doi:10.7554/eLife.28606

Conkar, D. and Firat-Karalar, E. N. (2020). Microtubule-associated proteins and emerging links to primary cilium structure, assembly, maintenance, and disassembly. *FEBS J.* **288**, 786-798. doi:10.1111/febs.15473

Conkar, D., Culfa, E., Odabasi, E., Rauniyar, N., Yates, J. R., III and Firat-Karalar, E. N. (2017). Centriolar satellite protein CCDC66 interacts with CEP290 and functions in cilium formation and trafficking. *J. Cell Sci.* **130**, 1450-1462. doi:10.1242/jcs.196832

Conkar, D., Bayraktar, H. and Firat-Karalar, E. N. (2019). Centrosomal and ciliary targeting of CCDC66 requires cooperative action of centriolar satellites, microtubules and molecular motors. *Sci. Rep.* **9**, 14250. doi:10.1038/s41598-019-50530-4

Das, A., Dickinson, D. J., Wood, C. C., Goldstein, B. and Slep, K. C. (2015). Crescerin uses a TOG domain array to regulate microtubules in the primary cilium. *Mol. Biol. Cell* **26**, 4248-4264. doi:10.1091/mbc.e15-08-0603

Dekomien, G., Vollrath, C., Petrasch-Parwez, E., Boevé, M. H., Akkad, D. A., Gerding, W. M. and Epplen, J. T. (2010). Progressive retinal atrophy in Schapendoes dogs: mutation of the newly identified CCDC66 gene. *Neurogenetics* **11**, 163-174. doi:10.1007/s10048-009-0223-z

den Hollander, A. I., Koenekoop, R. K., Mohamed, M. D., Arts, H. H., Boldt, K., Towns, K. V., Sedmak, T., Beer, M., Nagel-Wolfrum, K., McKibbin, M. et al. (2007). Mutations in LCA5, encoding the ciliary protein lebercilin, cause Leber congenital amaurosis. *Nat. Genet.* **39**, 889-895. doi:10.1038/ng2066

Drivas, T. G. and Bennett, J. (2014). CEP290 and the primary cilium. *Adv. Exp. Med. Biol.* **801**, 519-525. doi:10.1007/978-1-4614-3209-8_66

Farmer, V. J. and Zanic, M. (2021). TOG-domain proteins. *Curr. Biol.* **31**, R499-R501. doi:10.1016/j.cub.2021.01.039

Firat-Karalar, E. N., Rauniyar, N., Yates, J. R., III and Stearns, T. (2014). Proximity interactions among centrosome components identify regulators of centriole duplication. *Curr. Biol.* **24**, 664-670. doi:10.1016/j.cub.2014.01.067

Frikstad, K.-A. M., Molinari, E., Thoresen, M., Ramsbottom, S. A., Hughes, F., Letteboer, S. J. F., Gilani, S., Schink, K. O., Stokke, T., Geimer, S. et al. (2019). A CEP104-CSPP1 complex is required for formation of primary cilia competent in Hedgehog signaling. *Cell Rep.* **28**, 1907-1922.e6. doi:10.1016/j.celrep.2019.07.025

Garcia-Gonzalo, F. R. and Reiter, J. F. (2017). Open Sesame: how transition fibers and the transition zone control ciliary composition. *Cold Spring Harb. Perspect. Biol.* **9**, a028134. doi:10.1101/cshperspect.a028134

Gerding, W. M., Schreiber, S., Schulte-Middelmann, T., de Castro Marques, A., Atorf, J., Akkad, D. A., Dekomien, G., Kremers, J., Dermietzel, R., Gal, A. et al. (2011). Ccdc66 null mutation causes retinal degeneration and dysfunction. *Hum. Mol. Genet.* **20**, 3620-3631. doi:10.1093/hmg/ddr282

Gheiratmand, L., Coyaud, E., Gupta, G. D., Laurent, E. M. N., Hasegan, M., Prosser, S. L., Gonçalves, J., Raught, B. and Pelletier, L. (2019). Spatial and proteomic profiling reveals centrosome-independent features of centriolar satellites. *EMBO J.* **38**, e101109. doi:10.15252/embj.2018101109

Gonçalves, J. and Pelletier, L. (2017). The ciliary transition zone: finding the pieces and assembling the gate. *Mol. Cells* **40**, 243-253. doi:10.14348/molcells.2017.0054

Graser, S., Stierhof, Y.-D., Lavoie, S. B., Gassner, O. S., Lamla, S., Le Clech, M. and Nigg, E. A. (2007). Cep164, a novel centriole appendage protein required for primary cilium formation. *J. Cell Biol.* **179**, 321-330. doi:10.1083/jcb.200707181

Gupta, G. D., Coyaud, E., Gonçalves, J., Mojarad, B. A., Liu, Y., Wu, Q., Gheiratmand, L., Comartin, D., Tkach, J. M., Cheung, S. W. T. et al. (2015). A dynamic protein interaction landscape of the human centrosome-cilium interface. *Cell* **163**, 1484-1499. doi:10.1016/j.cell.2015.10.065

Gurkaslar, H. K., Culfa, E., Arslanhan, M. D., Lince-Faria, M. and Firat-Karalar, E. N. (2020). CCDC57 cooperates with microtubules and microcephaly protein CEP63 and regulates centriole duplication and mitotic progression. *Cell Rep.* **31**, 107630. doi:10.1016/j.celrep.2020.107630

He, M., Subramanian, R., Bangs, F., Omelchenko, T., Liem, K. F., Jr, Kapoor, T. M. and Anderson, K. V. (2014). The kinesin-4 protein Kif7 regulates mammalian Hedgehog signalling by organizing the cilium tip compartment. *Nat. Cell Biol.* **16**, 663-672. doi:10.1038/ncb2988

Jewett, C. E., Soh, A. W. J., Lin, C. H., Lu, Q., Lencer, E., Westlake, C. J., Pearson, C. G. and Prekeris, R. (2021). RAB19 directs cortical remodeling and membrane growth for primary ciliogenesis. *Dev. Cell* **56**, 325-340.e8. doi:10.1016/j.devcel.2020.12.003

Keeling, J., Tsiokas, L. and Maskey, D. (2016). Cellular mechanisms of ciliary length control. *Cells* **5**, 6. doi:10.3390/cells5010006

Kobayashi, T., Kim, S., Lin, Y.-C., Inoue, T. and Dynlacht, B. D. (2014). The CP110-interacting proteins Talpid3 and Cep290 play overlapping and distinct roles in cilia assembly. *J. Cell Biol.* **204**, 215-229. doi:10.1083/jcb.201304153

Kodani, A., Yu, T. W., Johnson, J. R., Jayaraman, D., Johnson, T. L., Al-Gazali, L., Sztriha, L., Partlow, J. N., Kim, H., Krup, A. L. et al. (2015). Centriolar satellites assemble centrosomal microcephaly proteins to recruit CDK2 and promote centriole duplication. *eLife* **4**, e07519. doi:10.7554/eLife.07519

Kohli, P., Höhne, M., Jüngst, C., Bertsch, S., Ebert, L. K., Schauss, A. C., Benzing, T., Rinschen, M. M. and Schermer, B. (2017). The ciliary membrane-associated proteome reveals actin-binding proteins as key components of cilia. *EMBO Rep.* **18**, 1521-1535. doi:10.15252/embr.201643846

Kubo, A., Sasaki, H., Yuba-Kubo, A., Tsukita, S. and Shiina, N. (1999). Centriolar satellites: molecular characterization, ATP-dependent movement toward centrioles and possible involvement in ciliogenesis. *J. Cell Biol.* **147**, 969-980. doi:10.1083/jcb.147.5.969

Latour, B. L., Van De Weghe, J. C., Rusterholz, T. D. S., Letteboer, S. J. F., Gomez, A., Shaheen, R., Gesemann, M., Karamzade, A., Asadollahi, M., Barroso-Gil, M. et al. (2020). Dysfunction of the ciliary ARMC9/TOGARAM1 protein module causes Joubert syndrome. *J. Clin. Invest.* **130**, 4423-4439. doi:10.1172/JCI131656

Lee, J. and Chung, Y. D. (2015). Ciliary subcompartments: how are they established and what are their functions? *BMB Rep.* **48**, 380-387. doi:10.5483/BMBRep.2015.48.7.084

Lu, Q., Insinna, C., Ott, C., Stauffer, J., Pintado, P. A., Rahajeng, J., Baxa, U., Walia, V., Cuenca, A., Hwang, Y.-S. et al. (2015). Early steps in primary cilium assembly require EHD1/EHD3-dependent ciliary vesicle formation. *Nat. Cell Biol.* **17**, 531. doi:10.1038/ncb3155

May, E. A., Kalocsay, M., D'Auriac, I. G., Schuster, P. S., Gygi, S. P., Nachury, M. V. and Mick, D. U. (2021). Time-resolved proteomics profiling of the ciliary Hedgehog response. *J. Cell Biol.* **220**, e202007207. doi:10.1083/jcb.202007207

Mellacheruvu, D., Wright, Z., Couzens, A. L., Lambert, J.-P., St-Denis, N. A., Li, T., Miteva, Y. V., Hauri, S., Sardiu, M. E., Low, T. Y. et al. (2013). The CRAPome:

a contaminant repository for affinity purification-mass spectrometry data. *Nat. Methods* **10**, 730-736. doi:10.1038/nmeth.2557

Mick, D. U., Rodrigues, R. B., Leib, R. D., Adams, C. M., Chien, A. S., Gygi, S. P. and Nachury, M. V. (2015). Proteomics of primary cilia by proximity labeling. *Dev. Cell* **35**, 497-512. doi:10.1016/j.devcel.2015.10.015

Mirvis, M., Stearns, T. and James Nelson, W. (2018). Cilium structure, assembly, and disassembly regulated by the cytoskeleton. *Biochem. J.* **475**, 2329-2353. doi:10.1042/BCJ20170453

Mirvis, M., Siemers, K. A., Nelson, W. J. and Stearns, T. P. (2019). Primary cilium loss in mammalian cells occurs predominantly by whole-cilium shedding. *PLoS Biol.* **17**, e3000381. doi:10.1371/journal.pbio.3000381

Mukhopadhyay, S. and Rohatgi, R. (2014). G-protein-coupled receptors, Hedgehog signaling and primary cilia. *Semin. Cell Dev. Biol.* **33**, 63-72. doi:10.1016/j.semcdb.2014.05.002

Murgiano, L., Becker, D., Spector, C., Carlin, K., Santana, E., Niggel, J. K., Jagannathan, V., Leeb, T., Pearce-Kelling, S., Aguirre, G. D. et al. (2020). CCDC66 frameshift variant associated with a new form of early-onset progressive retinal atrophy in Portuguese Water Dogs. *Sci. Rep.* **10**, 21162. doi:10.1038/s41598-020-77980-5

Nachury, M. V. (2018). The molecular machines that traffic signaling receptors into and out of cilia. *Curr. Opin. Cell Biol.* **51**, 124-131. doi:10.1016/j.ceb.2018.03.004

Nachury, M. V. and Mick, D. U. (2019). Establishing and regulating the composition of cilia for signal transduction. *Nat. Rev. Mol. Cell Biol.* **20**, 389-405. doi:10.1038/s41580-019-0116-4

Nachury, M. V., Loktev, A. V., Zhang, Q., Westlake, C. J., Peränen, J., Merdes, A., Slusarski, D. C., Scheller, R. H., Bazan, J. F., Sheffield, V. C. et al. (2007). A core complex of BBS proteins cooperates with the GTPase Rab8 to promote ciliary membrane biogenesis. *Cell* **129**, 1201-1213. doi:10.1016/j.cell.2007.03.053

Nager, A. R., Goldstein, J. S., Herranz-Pérez, V., Portran, D., Ye, F., Garcia-Verdugo, J. M. and Nachury, M. V. (2017). An actin network dispatches ciliary GPCRs into extracellular vesicles to modulate signaling. *Cell* **168**, 252-263.e14. doi:10.1016/j.cell.2016.11.036

Odabasi, E., Gul, S., Kavakli, I. H. and Firat-Karalar, E. N. (2019). Centriolar satellites are required for efficient ciliogenesis and ciliary content regulation. *EMBO Rep.* **20**, e47723. doi:10.15252/embr.201947723

Odabasi, E., Batman, U. and Firat-Karalar, E. N. (2020). Unraveling the mysteries of centriolar satellites: time to rewrite the textbooks about the centrosome/cilium complex. *Mol. Biol. Cell* **31**, 866-872. doi:10.1091/mbc.E19-07-0402

Patzke, S., Redick, S., Warsame, A., Murga-Zamalloa, C. A., Khanna, H., Doxsey, S. and Stokke, T. (2010). CSPP is a ciliary protein interacting with Nephrocystin 8 and required for cilia formation. *Mol. Biol. Cell* **21**, 2555-2567. doi:10.1091/mbc.e09-06-0503

Pedersen, L. B. and Akhmanova, A. (2014). Kif7 keeps cilia tips in shape. *Nat. Cell Biol.* **16**, 623-625. doi:10.1038/ncb2997

Pedersen, L. B., Schrøder, J. M., Satir, P. and Christensen, S. T. (2012). The ciliary cytoskeleton. *Compr. Physiol.* **2**, 779-803. doi:10.1002/cphy.c110043

Phua, S. C., Chiba, S., Suzuki, M., Su, E., Roberson, E. C., Pusapati, G. V., Setou, M., Rohatgi, R., Reiter, J. F., Ikegami, K. et al. (2017). Dynamic remodeling of membrane composition drives cell cycle through primary cilia excision. *Cell* **168**, 264-279.e15. doi:10.1016/j.cell.2016.12.032

Prevo, B., Scholey, J. M. and Peterman, E. J. G. (2017). Intraflagellar transport: mechanisms of motor action, cooperation, and cargo delivery. *FEBS J.* **284**, 2905-2931. doi:10.1111/febs.14068

Prosser, S. L. and Pelletier, L. (2020). Centriolar satellite biogenesis and function in vertebrate cells. *J. Cell Sci.* **133**, jcs239566. doi:10.1242/jcs.239566

Quanlong, L., Chuanmao, Z. and Westlake, C. (2021). Live-cell fluorescence imaging of ciliary dynamics. *Biophys. Rep.* **7**, 101-110. doi:10.52601/bpr.2021.210005

Quarantotti, V., Chen, J.-X., Tischer, J., Gonzalez Tejedo, C., Papachristou, E. K., D'Santos, C. S., Kilmartin, J. V., Miller, M. L. and Gergely, F. (2019). Centriolar satellites are acentriolar assemblies of centrosomal proteins. *EMBO J.* **38**, e101082. doi:10.15252/embj.2018101082

Reiter, J. F. and Leroux, M. R. (2017). Genes and molecular pathways underpinning ciliopathies. *Nat. Rev. Mol. Cell Biol.* **18**, 533-547. doi:10.1038/nrm.2017.60

Rezabkova, L., Kraatz, S. H. W., Akhmanova, A., Steinmetz, M. O. and Kammerer, R. A. (2016). Biophysical and structural characterization of the centriolar protein Cep104 interaction network. *J. Biol. Chem.* **291**, 18496-18504. doi:10.1074/jbc.M116.739771

Satish Tammana, T. V., Tammana, D., Diener, D. R. and Rosenbaum, J. (2013). Centrosomal protein CEP104 (Chlamydomonas FAP256) moves to the ciliary tip during ciliary assembly. *J. Cell Sci.* **126**, 5018-5029. doi:10.1242/jcs.133439

Schreiber, S., Petrasch-Parwez, E., Porrmann-Kelterbaum, E., Förster, E., Epplen, J. T. and Gerding, W. M. (2018). Neurodegeneration in the olfactory bulb and olfactory deficits in the Ccdc66 -/- mouse model for retinal degeneration. *IBRO Rep.* **5**, 43-53. doi:10.1016/j.ibror.2018.08.004

Sergouniotis, P. I., Chakarova, C., Murphy, C., Becker, M., Lenassi, E., Arno, G., Lek, M., MacArthur, D. G., Consortium, U. C.-E., Bhattacharya, S. S. et al. (2014). Biallelic variants in TTLL5, encoding a tubulin glutamylase, cause retinal dystrophy. *Am. J. Hum. Genet.* **94**, 760-769. doi:10.1016/j.ajhg.2014.04.003

Shannon, P., Markiel, A., Ozier, O., Baliga, N. S., Wang, J. T., Ramage, D., Amin, N., Schwikowski, B. and Ideker, T. (2003). Cytoscape: a software environment for integrated models of biomolecular interaction networks. *Genome Res.* **13**, 2498-2504. doi:10.1101/gr.1239303

Sharp, J. A., Plant, J. J., Ohsumi, T. K., Borowsky, M. and Blower, M. D. (2011). Functional analysis of the microtubule-interacting transcriptome. *Mol. Biol. Cell* **22**, 4312-4323. doi:10.1091/mbc.e11-07-0629

Szymanska, K. and Johnson, C. A. (2012). The transition zone: an essential functional compartment of cilia. *Cilia* **1**, 10. doi:10.1186/2046-2530-1-10

Tanos, B. E., Yang, H. J., Soni, R., Wang, W. J., Macaluso, F. P., Asara, J. M. and Tsou, M.-F. B. (2013). Centriole distal appendages promote membrane docking, leading to cilia initiation. *Genes Dev.* **27**, 163-168. doi:10.1101/gad.207043.112

Taschner, M. and Lorentzen, E. (2016). The intraflagellar transport machinery. *Cold Spring Harb. Perspect. Biol.* **8**, a028092. doi:10.1101/cshperspect.a028092

Tu, H.-Q., Qin, X.-H., Liu, Z.-B., Song, Z.-Q., Hu, H.-B., Zhang, Y.-C., Chang, Y., Wu, M., Huang, Y., Bai, Y.-F. et al. (2018). Microtubule asters anchored by FSD1 control axoneme assembly and ciliogenesis. *Nat. Commun.* **9**, 5277. doi:10.1038/s41467-018-07664-2

Wang, J. and Barr, M. M. (2016). Ciliary extracellular vesicles: txt msg organelles. *Cell. Mol. Neurobiol.* **36**, 449-457. doi:10.1007/s10571-016-0345-4

Westlake, C. J., Baye, L. M., Nachury, M. V., Wright, K. J., Ervin, K. E., Phu, L., Chalouni, C., Beck, J. S., Kirkpatrick, D. S., Slusarski, D. C. et al. (2011). Primary cilia membrane assembly is initiated by Rab11 and transport protein particle II (TRAPPII) complex-dependent trafficking of Rabin8 to the centrosome. *Proc. Natl. Acad. Sci. USA* **108**, 2759-2764. doi:10.1073/pnas.1018823108

Wheway, G., Nazlamova, L. and Hancock, J. T. (2018). Signaling through the Primary Cilium. *Front Cell Dev. Biol.* **6**, 8. doi:10.3389/fcell.2018.00008

Wiegering, A., Rüther, U. and Gerhardt, C. (2018). The ciliary protein Rpgrip1l in development and disease. *Dev. Biol.* **442**, 60-68. doi:10.1016/j.ydbio.2018.07.024

Wloga, D., Joachimiak, E., Louka, P. and Gaertig, J. (2017). Posttranslational modifications of tubulin and cilia. *Cold Spring Harb. Perspect. Biol.* **9**, a028159. doi:10.1101/cshperspect.a028159

Yamazoe, T., Nagai, T., Umeda, S., Sugaya, Y. and Mizuno, K. (2020). Roles of TOG and jelly-roll domains of centrosomal protein CEP104 in its functions in cilium elongation and Hedgehog signaling. *J. Biol. Chem.* **295**, 14723-14736. doi:10.1074/jbc.RA120.013334

Figure S1

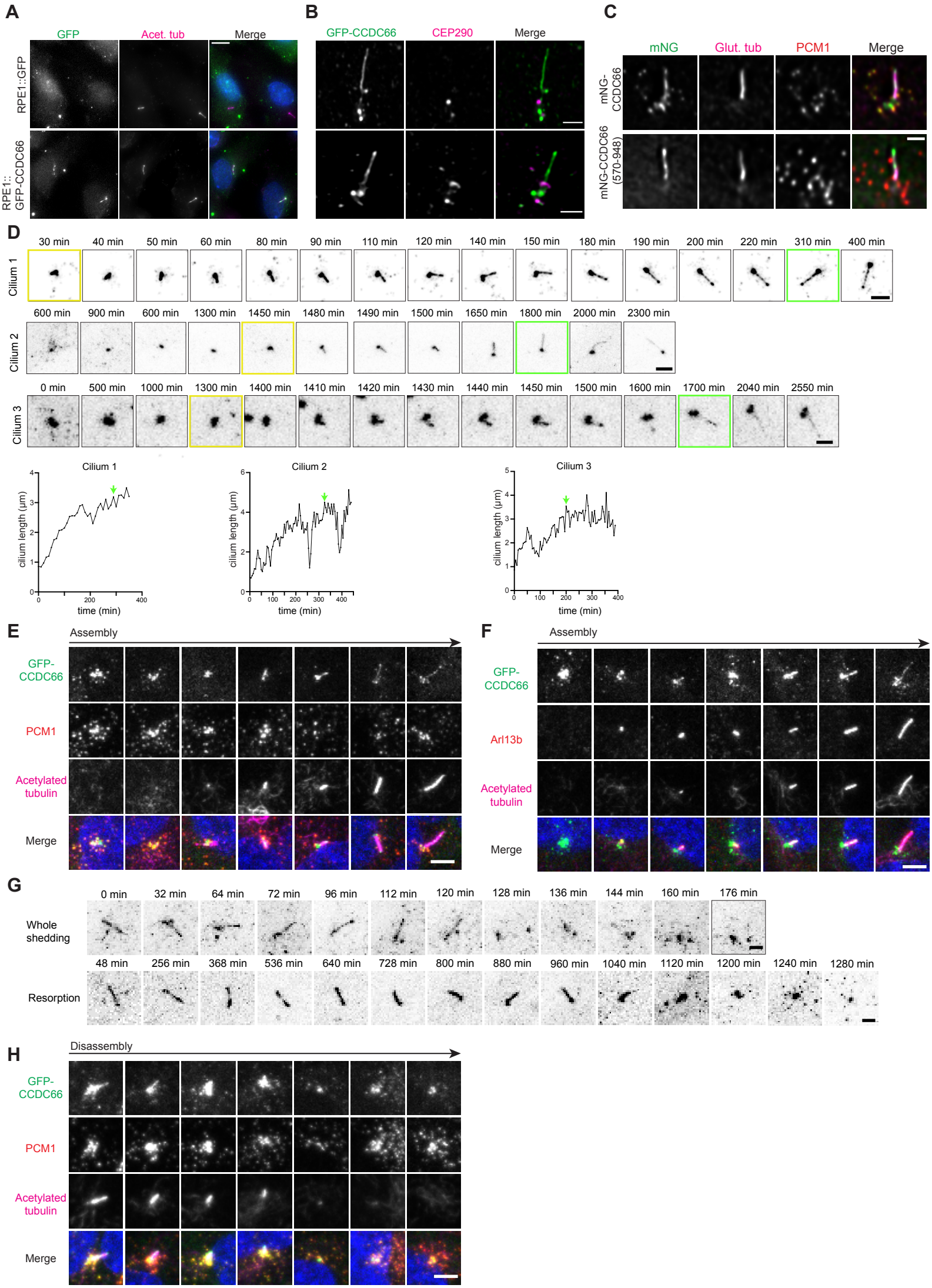

Fig. S1. (A) Ciliary localization of GFP-CCDC66 in RPE1 cells is specific
RPE1::GFP and RPE1::GFP-CCDC66 cells were serum starved for 24 hours and fixed with methanol and stained for GFP and acetylated tubulin antibodies along with DAPI in order to visualize DNA. Scale bar: 10μm

(B) Superresolution imaging of ciliary GFP-CCDC66 with CEP290
RPE1::GFP-CCDC66 cells were serum starved for 24 hours and fixed with methanol and stained for GFP and CEP290 antibodies. Images were acquired with SIM. Scale bar: 3μm.

(C) C-terminal microtubule binding fragment (570-948 a.a.) of CCDC66 localizes to the basal body and the axoneme but not centriolar satellites. RPE1::mNeonGreen (mNG)-CCDC66 and RPE1::mNG-CCDC66 (570-948) cells were serum starved for 48 hours, fixed and stained for mNeonGreen, glutamylated tubulin and PCM1 or acetylated tubulin and gamma tubulin antibodies. Scale bar: 2μm

(D) Spatiotemporal localization dynamics of CCDC66 during cilium assembly. RPE1::GFP-CCDC66 cells were plated onto Lab-Tek imaging dish at 100% confluency and started to be imaged with confocal microscopy every 10 min immediately after serum starvation. Representative images are from three different cells that form primary cilia. GFP signal is inverted and represented as black onto white background for ciliary and centriolar satellite pools of CCDC66 to be distinguished. Below graphs represent the cilium length over the course of imaging from these three cilia. Cilium length was measured starting from the yellow framed time points. Green framed time points and the green arrow represent reaching the steady state cilium. Scale bar: 2μm

(E and F) CCDC66 localization with respect to centriolar satellite, centrosome and ciliary markers during cilium assembly. RPE1::GFP-CCDC66 cells were serum starved for 24 hours and fixed with methanol and stained for **(E)** GFP, PCM1, acetylated tubulin or **(F)** GFP, ARL13B and acetylated tubulin antibodies along with DAPI in order to visualize DNA. Images from left to right represent CCDC66 localization during the initiation and elongation phases of primary cilium formation. Scale bar: 5μm

(G) Spatiotemporal localization dynamics of CCDC66 during cilium disassembly.
RPE1::GFP-CCDC66 cells were plated onto Lab-Tek imaging dish at 100% confluency, serum starved for 48 hours to induce cilium formation, and started to be imaged with confocal microscopy every 10 min immediately after serum addition. Representative images are from two cilia that undergo cilium disassembly by whole cilium shedding and resorption. GFP signal is inverted and represented as black onto white background for ciliary and centriolar satellite pools of CCDC66 to be distinguished. Scale bar: 2μm

(H) CCDC66 localization with respect to centriolar satellite, centrosome and ciliary markers during cilium disassembly After 24h serum starvation**,** RPE1::GFP-CCDC66 cells were incubated with complete media for 24 hours and fixed with methanol and stained for GFP, PCM1, acetylated tubulin along with DAPI in order to visualize DNA. Images from left to right represent CCDC66 localization during the shortening and disassembly of phases of primary cilium formation. Scale bar: 5μm

Figure S2

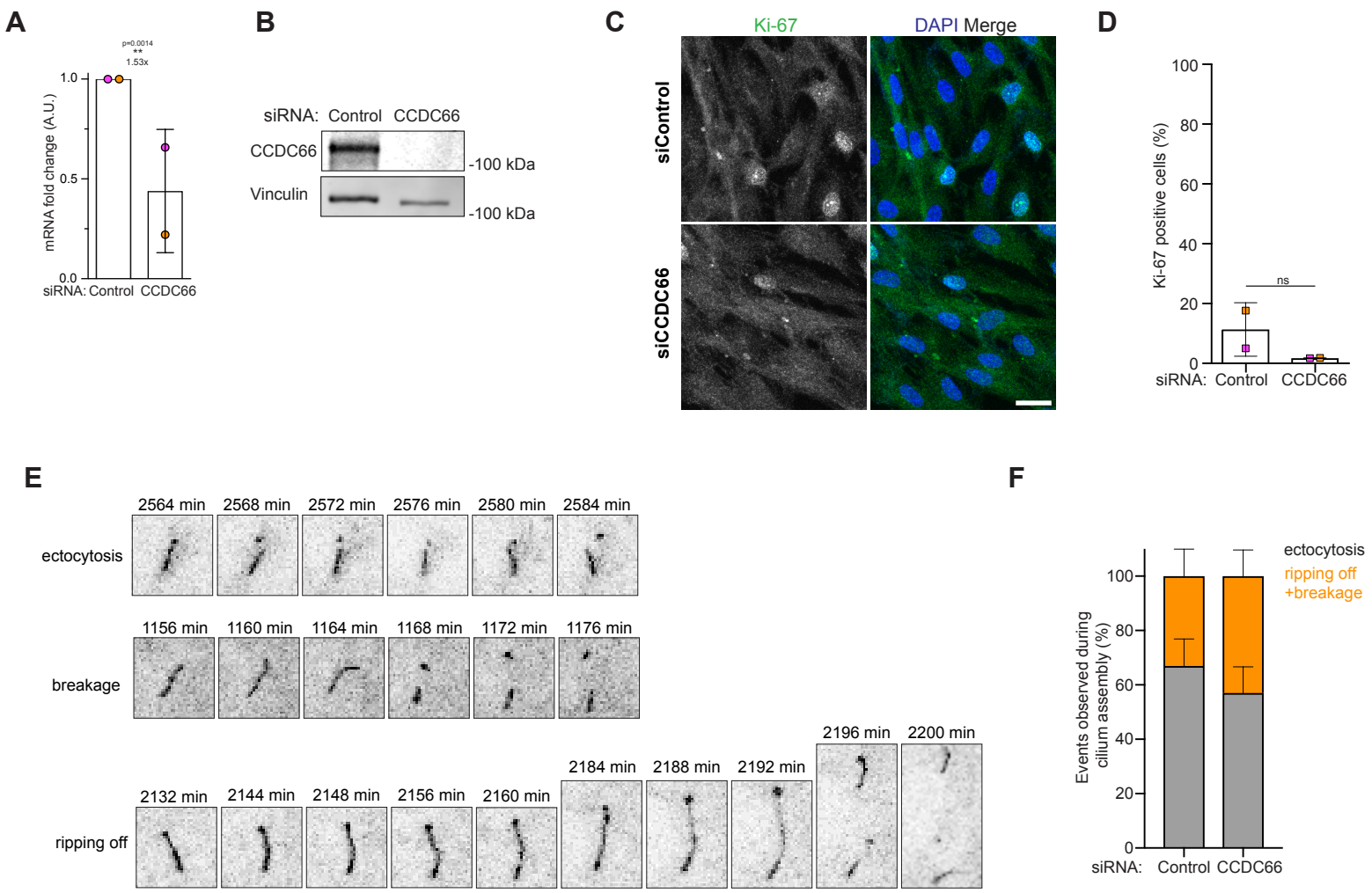

Fig. S2. (A-B) Validation of CCDC66 depletion. RPE1 cells were transfected with two rounds control or CCDC66 siRNA. 48 hours later, they were collected and processed for **(A)** qPCR analysis and **(B)** immunoblotting with CCDC66 and vinculin as control loading control. Graph represents CCDC66 mRNA fold change relative to control depletion condition. (*P < 0.5, t-test)

(C and D) Effects of CCDC66 depletion on the percentage of quiescent cells. RPE1 cells were transfected with two rounds of control or CCDC66 siRNA and serum starved for 24 hours. **(C)** Following fixation with methanol, cells were stained for anti-Ki67 and DAPI for visualization of DNA. **(D)** Graph indicates percentage of Ki-67 positive cells. Data represent the mean ±SD. Scale bar: 15μm.

(E-F) Effects of CCDC66 depletion on steady-state cilia. (C) Control or CCDC66 depleted RPE1::mCitrine-Smoothened cells were imaged after serum starvation. Cilia from both conditions were observed to undergo ectocytosis, breakage and ripping off events during cilium assembly. Images representing these events are given. **(D)** Graph indicates the percentage of ectocytosis (grey) and breakage+ripping off (orange) events in control and CCDC66 depleted cells. Data represents the mean ±SD. (100 cells/experiment, *P < 0.5, t-test)

Figure S3

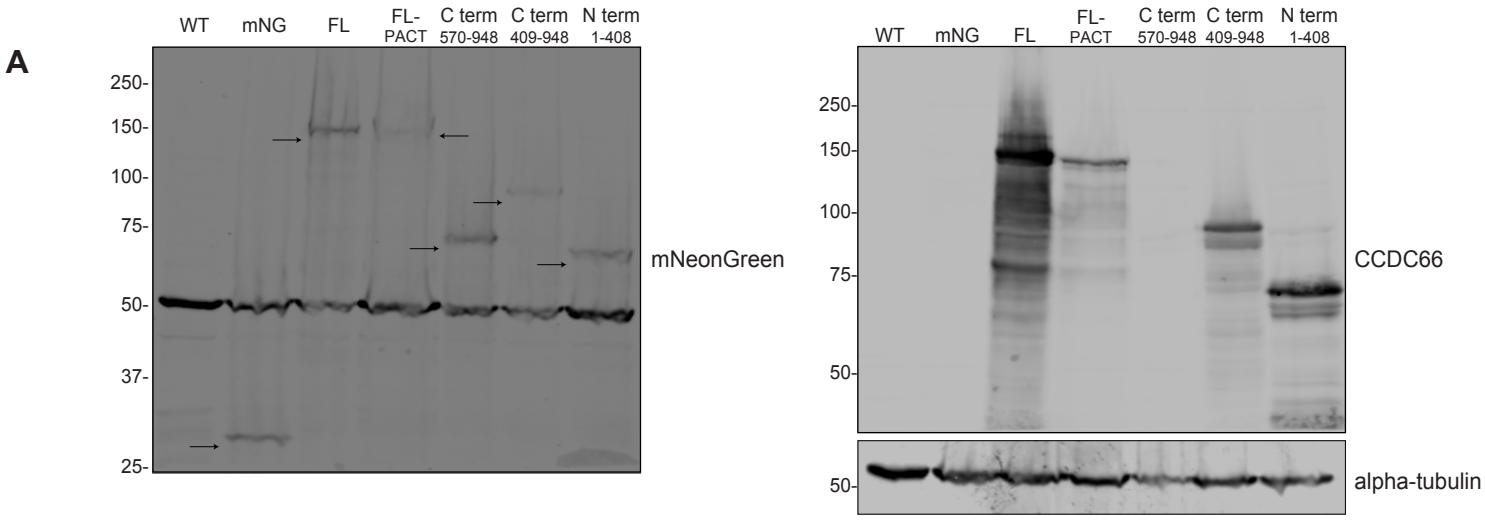

Fig. S3. (A) Validation of stable protein expression. RPE1 cell lines expressing mNeonGreen, mNeonGreen tagged CCDC66 full length, CCDC66-PACT and CCDC66 C terminal (570-948), CCDC66 (409-948) and CCDC66 (1-408) were processed and immunoblotted for mNeonGreen, CCDC66 and alpha tubulin antibodies. Black arrows indicate the corresponding band for NG tagged protein.

(B) mNG-CCDC66-PACT fusion protein localization is restricted to the basal body. RPE1 cells stably expressing mNeonGreen-CCDC66-PACT were serum starved for 48 hours. Following fixation, cells were stained for mNeonGreen, acetylated tubulin, gamma tubulin antibodies or mNeonGreen, glutamylated tubulin, PCM1 and DAPI for visualization of DNA. Scale bar: 2μm.

(C) mNG-CCDC66-PACT expression change centrosomal levels of centrosome and satellite proteins. RPE1::mNG-CCDC66 and RPE1::mNG-CCDC66-PACT cells were fixed and stained with CEP290, CEP63, PCM1, CEP131 and centrin3 along with centrosomal marker gamma tubulin. Gamma tubulin is taken as reference to quantify centrosomal levels of indicated proteins. Data represent the mean ±SD. Magenta and orange represent individual values from two independent experiments. (35 cell/ experiment, ns: not significant, t-test) Scale bar: 10μm

Figure S4

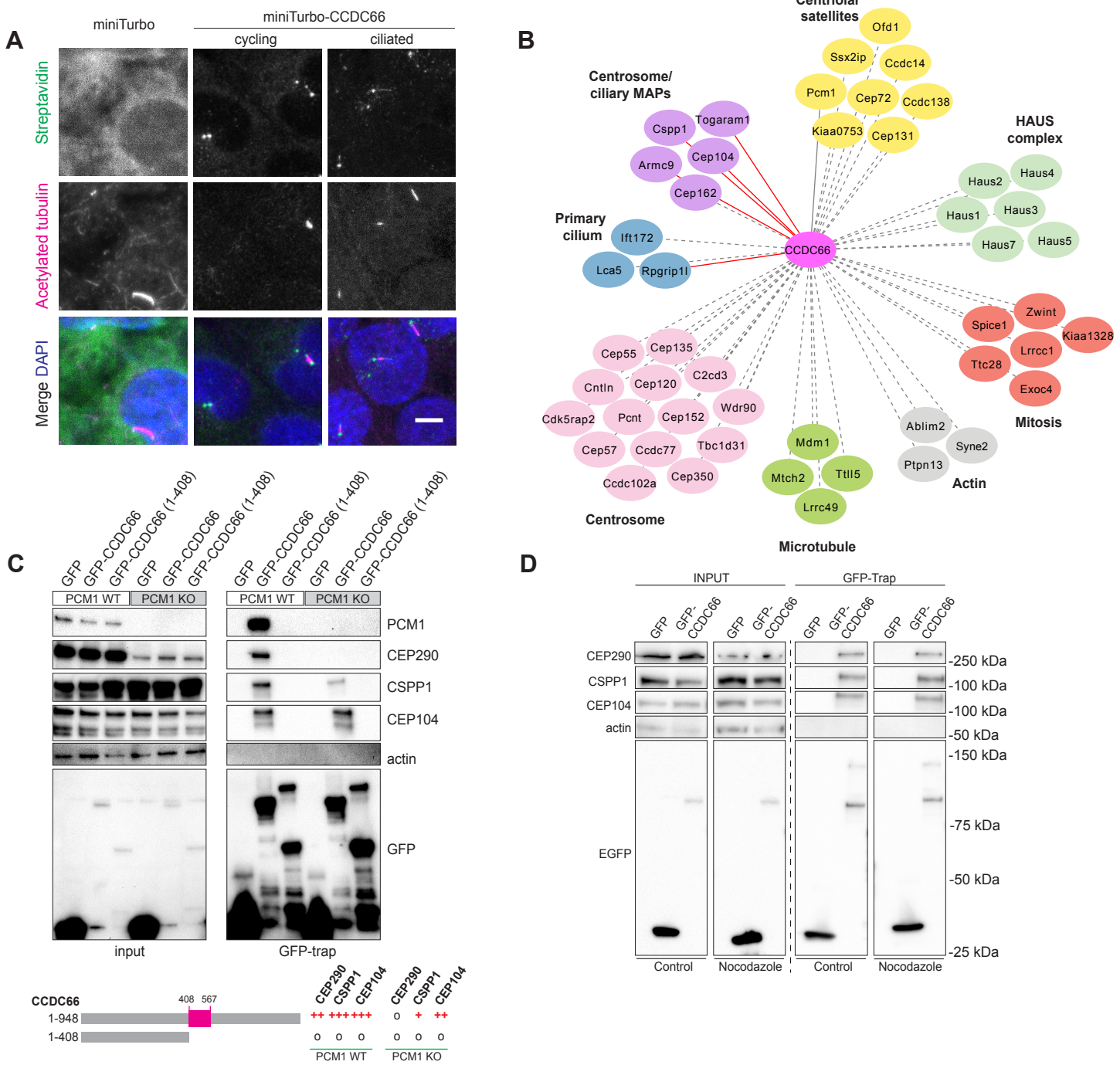

Fig. S4. (A) miniTurbo-CCDC66 induces localized biotinylation at the centrosome, centriolar satellites and primary cilium. 100% confluency IMCD3 cells stably expressing miniTurboID or miniTurboID-CCDC66 were serum starved for 48 hours. Both cell populations were treated with 500 µM biotin for 30 minutes and fixed with methanol. Cells were stained for anti-acetylated tubulin, Streptavidin and DAPI. Scale bar: 5µm

(B) CCDC66 proximity interaction map in ciliated cells. Final ciliated CCDC66 proximity interactome list is generated after applying several filtering steps to remove unspecific proteins using NSAF values. Remaining proteins are categorized based on their function and localization information**.** Dashed line: proximity interaction, solid red line: proximity and direct interactor.

(C) Centriolar satellites regulate interaction between CCDC66 and CEP290, CEP104 and CSPP1. PCM1 wild type (WT) and knockout (KO) HEK293T cells were transfected with EGFP, EGFP-CCDC66 full length and EGFP-CCDC66 (1-408) constructs. 2 days after transfection, cells were collected, lysed, and subjected to pull down with GFP Trap beads. Input and pellet were immunoblotted with anti GFP, PCM1, CEP290, CSPP1, CEP104 and actin as a control. The schematics summarizes the results of the pull down (o: no interaction, +: weak interaction, + +: moderate interaction, +++: strong interaction).

(D) CCDC66 interacts CEP290, CSPP1 and CEP104 independent of microtubules. HEK293T cells were transfected with EGFP or EGFP-CCDC66 full length. 2 days after transfection, cells were treated with 5 ug/ml nocodazole or 0.02% DMSO as a control. Following incubation, cells were collected, lysed, and subjected to pull down with GFP Trap beads. Input and pellet were immunoblotted with anti GFP, CEP290, CSPP1, CEP104 and actin as a control.

(E) Validation of CEP104 and CSPP1 depletion with Western Blotting. RPE1 cells were transfected with two rounds of control, CEP104 or CSPP1 siRNAs. 72 hours after first transfection, cells were collected, lysed and blotted for CSPP1, CEP104 and alpha tubulin antibodies.

(F-H) Validation of CEP104 and CSPP1 depletion by functional assays. RPE1 cells were transfected with two rounds of control, CCDC66, CSPP1 or CEP104 siRNAs and serum starved for 48 hours. Following fixation with methanol, cells were stained for acetylated tubulin and DAPI for visualization of DNA. **(F)** Percentage of cilium formation and **(G)** ciliary length were plotted. (100 cell or cilia /experiment, *P < 0.5, **P < 0.01, ***P < 0.001, ****P < 0.0001, ns: not significant, two way ANOVA) Scale bar: 10µm

(I-J) CCDC66 depletion causes cilium formation defect in RPE1::mNG-CEP104 and RPE1::mNG-CSPP1 cell lines. (I) RPE1::mNG-CEP104 or (J) RPE1::mNG-CSPP1 cells were transfected with two rounds of control or CCDC66 siRNA and serum starved for 48 hours. Percentage of cilium formation was quantified by dividing the cilium number determined by counting ARL13b by total cell number determined by counting nuclei and plotted. Magenta and orange represent individual values from two independent experiments. Error bars represent ±SD. (100 cells/serum starvation time point for each experiment, *P < 0.05, **P < 0.01, t-test

Table S1. Mass spectrometry results of proximity interactors of miniTurboID and miniTurboID-CCDC66 in ciliated IMCD3 cells, related to Supplementary Figure 4A and B. Column explanations of raw data are placed to sheet 2.

Click here to download Table S1

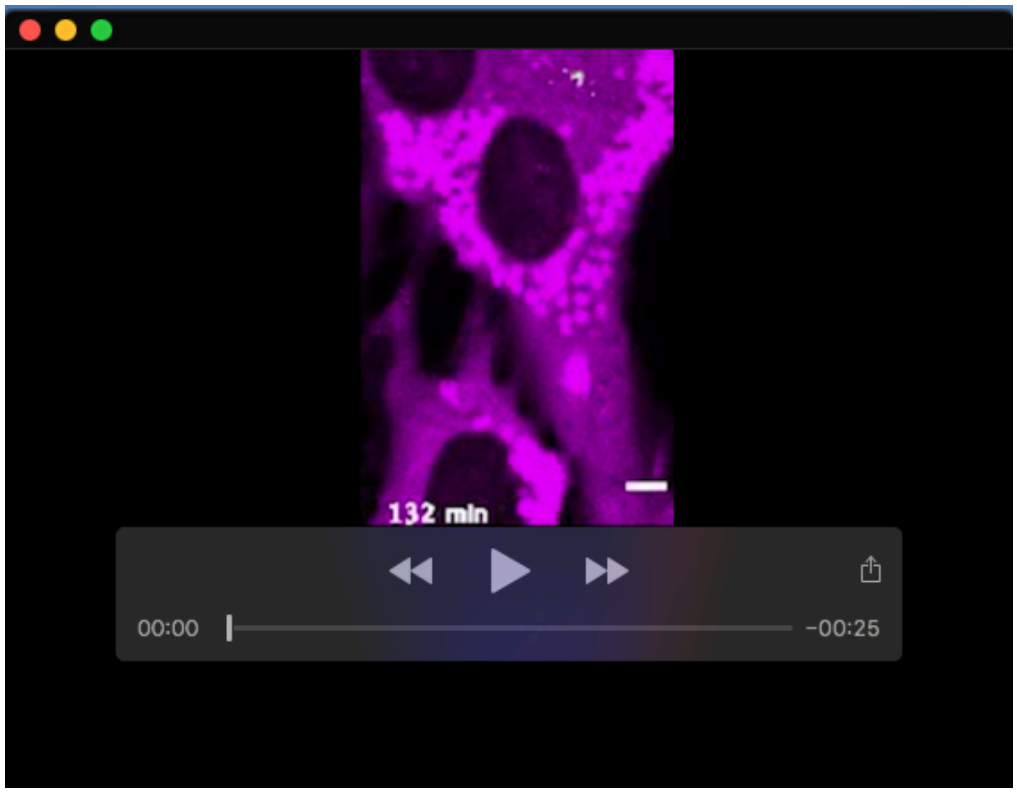

Movie 1. CCDC66 dynamic localization during cilium assembly.
RPE1::mNeonGreen-CCDC66, mScarlet-ARL13B cells were imaged with confocal microscopy every 8 minutes immediately after serum starvation. Scale bar: 5μm**.**

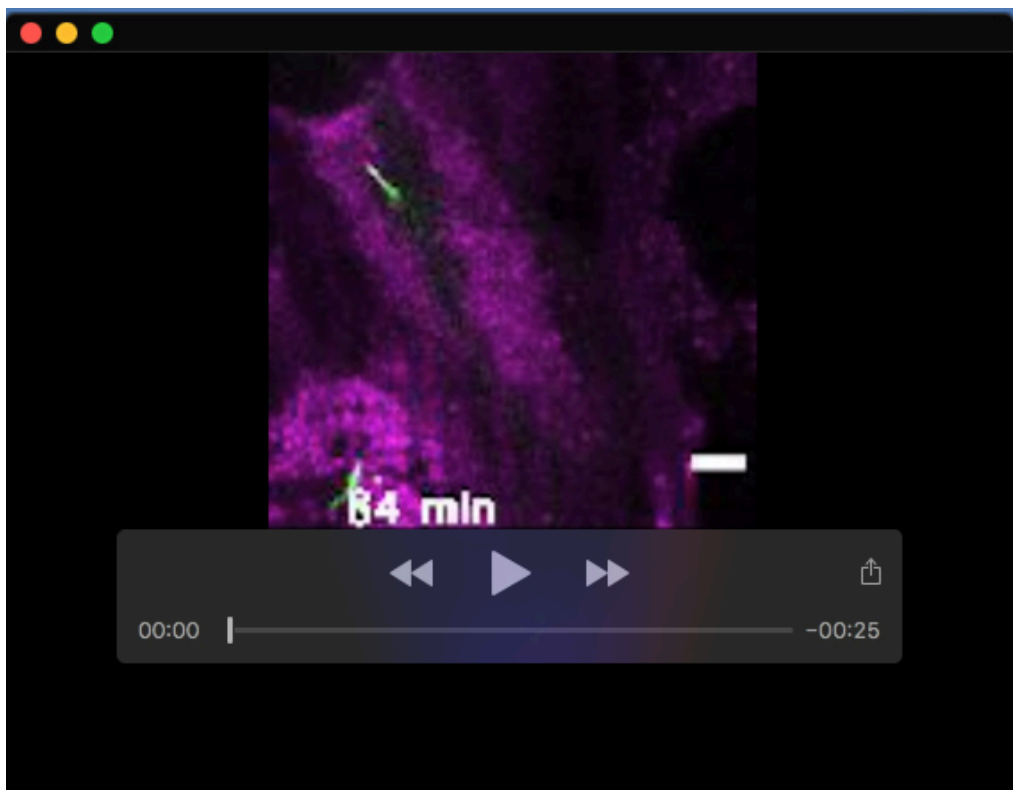

Movie 2. CCDC66 dynamic localization during cilium disassembly. After 48 hours serum starvation, RPE1::mNeonGreen-CCDC66, mScarlet-ARL13B cells were imaged with confocal microscopy every 6 minutes immediately upon serum addition. Scale bar: 5-μm.